National Library of Canada
Bibliothèque nationale du Canada

Canadian Theses Service
Service des thèses canadiennes

Ottawa, Canada
K1A 0N4

NOTICE

The quality of this microform is heavily dependent upon the quality of the original thesis submitted for microfilming. Every effort has been made to ensure the highest quality of reproduction possible.

If pages are missing, contact the university which granted the degree.

Some pages may have indistinct print especially if the original pages were typed with a poor typewriter ribbon or if the university sent us an inferior photocopy.

Reproduction in full or in part of this microform is governed by the Canadian Copyright Act, R.S.C. 1970, c. C-30, and subsequent amendments.

AVIS

La qualité de cette microforme dépend grandement de la qualité de la thèse soumise au microfilmage. Nous avons tout fait pour assurer une qualité supérieure de reproduction.

S'il manque des pages, veuillez communiquer avec l'université qui a conféré le grade.

La qualité d'impression de certaines pages peut laisser à désirer, surtout si les pages originales ont été dactylographiées à l'aide d'un ruban usé ou si l'université nous a fait parvenir une photocopie de qualité inférieure.

La reproduction, même partielle, de cette microforme est soumise à la Loi canadienne sur le droit d'auteur, SRC 1970, c. C-30, et ses amendements subséquents.

NL-339 (r. 88/04) c

Canada

THE UNIVERSITY OF ALBERTA

EVALUATION OF FILTERS FOR SINGLE PHOTON EMISSION COMPUTED TOMOGRAPHY

by

ATSUSHI M. TAKAHASHI

A THESIS

SUBMITTED TO THE FACULTY OF GRADUATE STUDIES AND RESEARCH

IN PARTIAL FULFILMENT OF THE REQUIREMENTS FOR THE DEGREE

OF Master of Science

IN

Medical Physics

Department of Physics

EDMONTON, ALBERTA

SPRING 1989

National Library of Canada
Bibliothèque nationale du Canada

Canadian Theses Service
Service des thèses canadiennes

Ottawa, Canada
K1A 0N4

The author has granted an irrevocable non-exclusive licence allowing the National Library of Canada to reproduce, loan, distribute or sell copies of his/her thesis by any means and in any form or format, making this thesis available to interested persons.

The author retains ownership of the copyright in his/her thesis. Neither the thesis nor substantial extracts from it may be printed or otherwise reproduced without his/her permission.

L'auteur a accordé une licence irrévocable et non exclusive permettant à la Bibliothèque nationale du Canada de reproduire, prêter, distribuer ou vendre des copies de sa thèse de quelque manière et sous quelque forme que ce soit pour mettre des exemplaires de cette thèse à la disposition des personnes intéressées.

L'auteur conserve la propriété du droit d'auteur qui protège sa thèse. Ni la thèse ni des extraits substantiels de celle-ci ne doivent être imprimés ou autrement reproduits sans son autorisation.

ISBN 0-315-52844-3

Canada

THE UNIVERSITY OF ALBERTA

RELEASE FORM

NAME OF AUTHOR: Atsushi M. Takahashi

TITLE OF THESIS: Evaluation of Filters for Single Photon Emission Computed Tomography

DEGREE: Master of Science

YEAR THIS DEGREE GRANTED: 1989

Permission is hereby granted to THE UNIVERSITY OF ALBERTA LIBRARY to reproduce single copies of this thesis and to lend or sell such copies for private, scholarly or scientific research purposes only.

The author reserves other publication rights, and neither the thesis nor extensive extracts from it may be printed or otherwise reproduced without the author's written permission.

Atsushi Takahashi
(Student's signature)

4828-122A street
Edmonton, Alberta

Date: April 26, 1989

THE UNIVERSITY OF ALBERTA

FACULTY OF GRADUATE STUDIES AND RESEARCH

The undersigned certify that they have read, and recommend to the Faculty of Graduate Studies and Research for acceptance, a thesis entitled

EVALUATION OF FILTERS FOR

SINGLE PHOTON EMISSION COMPUTED TOMOGRAPHY

submitted by Atsushi M. Takahashi in partial fulfilment of the requirements for the degree of Master of Science in Medical Physics.

.....
Co-Supervisor

.....
Co-Supervisor

.....

.....

Date: April 24, 1989

Abstract

Digital signal processing procedures have become an important part of Single Photon Emission Computed Tomography (SPECT) reconstruction. By optimizing the projection images, the quality of the reconstructed images is expected to improve. In the past the Butterworth filter has been used to suppress noise. Recently, an image dependent Metz filter which combines resolution recovery with noise suppression has been implemented in clinical studies. Much can be gained, especially with medium energy isotopes, through the use of a resolution recovery filter.

Various experiments have been performed to study the effects of different imaging parameters and processing techniques. The noise in flood tank phantom images was analyzed. A special test phantom with various inserts was constructed and used for contrast measurements and in a comparison test, in which images were compared to standard, reference images. Several sets of technetium-99m and indium-111 images were acquired under different experimental conditions. The images were filtered using the Butterworth and image dependent Metz filters. The tests demonstrate that the Metz filter significantly improves all the images acquired under clinical SPECT conditions.

Table of Contents

Chapter I Introduction

1.1 Introduction to Thesis 1

1.2 Introduction to Nuclear Medicine 2

1.2.1 General 2

1.2.2 Radionuclides 3

Chapter II Anger Scintillation Camera

2.1 General 5

2.2 Camera parameters 5

2.3 Parts of an Anger Camera 6

2.3.1 Collimator 8

2.3.2 Scintillation Crystal 10

2.3.3 Light Pipe 11

2.3.4 Photomultiplier Tubes 11

2.3.5 Amplifiers and Electrical Weighting Network . 12

2.3.5.1 Temporal Resolution and Detector Saturation 13

2.3.6 Computer Interface 16

2.4 Photoelectric Absorption and Compton Scatter 17

Chapter III SPECT

3.1 Definition and Description of SPECT 20

3.2 Reconstruction Mathematics 21

Chapter IV Image Processing in the Fourier Domain (Filtering)

4.1 System Response and Image Characteristics 25

4.2 Fourier Techniques 26

4.3 Image Characteristics 29

4.4 Noise 30

4.5 Distance and Scatter 32

4.6 Filter Theory 32

4.7 Actual Filters 35

Chapter V Experiments

5.1 Objectives 41

5.2 Apparatus 42

5.3 Procedure for the Acquisition of Images 45

5.3.1 Experiment I 45

5.3.1.1 Part a 45

5.3.1.2 Part b 45

5.3.2 Experiment II 48

5.3.2.1 Part a 48

5.3.2.2 Part b 49

5.4 Procedure for Filtering Test Phantom Images 49

5.5 Procedure for Analysis of Images 50

5.5.1 Noise 51

5.5.2 Contrast 51

5.5.3 Comparison to Reference Image 52

5.6 Results 55

5.6.1 Noise 55

5.6.2 Contrast 55

5.6.3 Comparison Test 55

5.7 Discussion of Results 81

5.7.1 Noise 81

5.7.2 Contrast and Comparison Tests 83

Chapter VI Conclusions and Future Experiments

6.1 Conclusion 93

6.2 Future Developments 95

Bibliography 97

Appendix I GE 400A Camera Specifications 99

List of Tables

Table		Page
5.1	Imaging parameters for ^{99m}Tc study.	48
5.2	Imaging parameters for ^{111}In study.	50

List of Figures

Figure		Page
2.1	Block diagram of an Anger scintillation camera.	7
2.2	Cross section of a parallel hole collimator.	9
2.3	Technetium-99m spectrum from GE camera.	14
2.4	Indium-111 spectrum from GE camera.	15
2.5	Compton Scattering.	18
3.1	The relationship of the camera and patient co-ordinate system.	21
3.2	Co-ordinate system used to describe the Fourier Slice Theorem.	23
4.1	Response of a system.	26
4.2	Contrast is measured as the signal to background ratio.	29
4.3	Point spread function and modulation transfer function for the LEGP and the MESP collimators.	31
4.4	Effect of scatter material on the point spread function and the modulation transfer function.	33
4.5	Butterworth filter with $F_C/F_N = 0.48$ and $n = 12.5$	36
4.6	Metz filter implemented for various images.	38
4.7	Log of the image's power spectrum used to determine the X parameter of an image dependent Metz filter.	39
5.1	Top and cross sections of test phantom.	44
5.2	Experimental setup.	46
5.3	Standard deviation of pixel counts for raw and filtered, technetium flood tank images.	56

5.4 Standard deviation of pixel counts for raw and filtered, indium flood tank images. 57

5.5 Photograph of Technetium filled test phantom reference image with raw, Butterworth filtered, and Metz filtered images acquired to 100 thousand and 1 million counts. 58

5.6 Photograph of Indium filled test phantom reference image with raw, Butterworth filtered, and Metz filtered images acquired to 100 thousand and 500 thousand counts. 59

5.7 Hot and cold spot contrast for technetium filled test phantom reference image. 60

5.8 Hot and cold spot contrast of technetium filled test phantom images acquired at camera face plotted for various counts. 61

5.9 Hot and cold spot contrast for 10 million count, technetium filled test phantom images acquired with 5.5cm scatter material plotted for various distances. 62

5.10 Hot and cold spot contrast for 10 million count, technetium filled test phantom images acquired at 20cm plotted for various amounts of scatter material. 63

5.11 Hot and cold spot contrast for 10 million count, technetium filled test phantom images acquired at camera face filtered with Butterworth and Metz filters. 64

5.12 Hot and cold spot contrast for 100 thousand count, technetium filled test phantom images acquired at camera face filtered with Butterworth and Metz filters. 65

5.13 Hot and cold spot contrast for 100 thousand count, technetium filled test phantom images acquired at 10cm with 5.5cm scatter material filtered with Butterworth and Metz filters. 66

5.14 Hot and cold spot contrast for 100 thousand count, technetium filled test phantom images acquired at 20cm with 11cm scatter material filtered with Butterworth and Metz filters. 67

5.15 Hot and cold spot contrast for indium filled test phantom reference image. 68

5.16 Hot and cold spot contrast of indium filled test phantom images acquired at camera face plotted for various counts. 69

5.17 Hot and cold spot contrast for 10 million count, indium filled test phantom images acquired with 5.5cm scatter material plotted for various distances. 70

5.18 Hot and cold spot contrast for 10 million count, indium filled test phantom images acquired at 20cm plotted for various amounts of scatter material. 71

5.19 Hot and cold spot contrast for 10 million count, indium filled test phantom images acquired at camera face filtered with Butterworth and Metz filters. 72

5.20 Hot and cold spot contrast for 100 thousand count, indium filled test phantom images acquired at camera face filtered with Butterworth and Metz filters. 73

5.21 Hot and cold spot contrast for 100 thousand count, indium filled test phantom images acquired at 11cm with 5.5cm scatter material filtered with Butterworth and Metz filters. 74

5.22 Hot and cold spot contrast for 100 thousand count, indium filled test phantom images acquired at 20cm with 11cm scatter material filtered with Butterworth and Metz filters. 75

5.23 Comparison factor for raw technetium filled test phantom images acquired under various conditions plotted as a function of counts. 76

5.24 Effect of Butterworth and Metz filters on comparison factor of technetium filled test phantom images. 77

5.25 Improvement index of Butterworth and Metz filtered, technetium filled test phantom images. 78

5.26 Comparison factor for raw indium filled test phantom images acquired under various conditions plotted as a function of counts. 79

5.27 Effect of Butterworth and Metz filters on comparison factor of indium filled test phantom images. 80

5.28 Improvement index of Butterworth and Metz filtered, indium filled test phantom images. 82

5.29 Unit step response of a) Butterworth filter, b) low energy collimator Metz filters, and c) medium energy collimator Metz filters. 87

Chapter I Introduction

1.1 Introduction to Thesis

In nuclear medicine, a biologically significant chemical or drug is labeled with a radioactive isotope and is injected into a patient to diagnose or treat disease. The earliest nuclear medicine procedures involved the measurement of gamma ray flux using a detector placed close to the skin of a patient injected with a radioactive material. Later, imaging became possible with the development of the rectilinear scanner. In 1958, the gamma camera or Anger camera, named after H. Anger, was developed. This gamma camera has become an important tool in nuclear medicine imaging. Most recently, the gamma camera has been used to acquire images which can be reconstructed to generate three dimensional tomographic images.

Due to the physical processes involved, the quality of nuclear medicine images may be poor, and much can be gained by utilizing standard image processing techniques. Often in the past the performance of these image processing techniques has been evaluated subjectively. The purpose of this study has been to develop quantitative measures of performance for image processing techniques used as part of the reconstruction process for nuclear medicine tomographic images.

This thesis will start with a brief introduction to the field of diagnostic nuclear medicine imaging. In chapter II, the terms used to evaluate the quality of images will be defined. In addition, the camera used to acquire nuclear medicine images will be described, and

some problems associated with its use will be discussed. A technique called Single Photon Emission Computed Tomography will be discussed in chapter III. Image processing techniques used to improve the quality of nuclear medicine images will be discussed in chapter IV. Various experiments used to study the effects of different imaging parameters and processing techniques will be described in detail in chapter V. Three quantitative tests used to evaluate image quality will also be introduced, and used to analyze the experimental results. Chapter VI will summarize and conclude the thesis.

1.2 Introduction to Nuclear Medicine

1.2.1 General

"A central premise of medicine is that all biological activity is the result of biochemical reactions and that for every pathology, there is an underlying biochemical defect." [Te80]

Diagnostic nuclear medicine maps biochemical and metabolic processes that may reveal the presence of disease. This is done by injecting the patient with a small amount of a chemical which is labeled with a radionuclide. This compound is called a radio pharmaceutical. The labeled pharmaceutical is usually administered in trace amounts too small to have any pharmacological effect. Typically, less than 1 mg of a pharmaceutical is administered. This small amount of drug is metabolized by the body. After a period of time, the pharmaceutical localizes in one or more organs. An appropriate pharmaceutical must be chosen so that the desired organ and metabolic function may be imaged. For example, if the structures

inside the brain are to be imaged, then a pharmaceutical that can cross the blood brain barrier is needed. The pharmaceutical must have a different distribution in the normal and the abnormal case. After the radio pharmaceutical is injected and time for localization has elapsed, the organ is imaged and the function of the organ is evaluated.

There are advantages of nuclear medicine over other imaging modalities. Since the nuclide is bonded to a drug, nuclear medicine imaging measures the metabolism or function of an organ or organ system. Other imaging modalities such as ultrasound or X-ray imaging measure morphology rather than function. The drug injected in a nuclear medicine process is in such small quantities that allergic or other reactions to the drug occur only very rarely. The contrast media used in conjunction with X-ray imaging are much more likely to cause unpleasant reactions.

The radiation dose delivered to the patient depends on several factors including the decay characteristics of the radionuclide, the amount of activity injected, and the way in which the body metabolizes the drug. In general, the radiation dose received by the patient in a nuclear medicine procedure is about the same as the dose from a conventional X-ray procedure such as a chest X-ray.

1.2.2 Radionuclides

Technetium-99m is a radionuclide that is routinely used in nuclear medicine. It has a half life of 6.03 hours. Technetium-99m emits a 140keV gamma ray. A photon of this energy has a half value

thickness of about 5cm in muscle tissue, but only about 0.3cm in sodium iodide. This means that the photons can pass through the body fairly easily but yet are easily detected outside the body.

There are various drugs that can be labeled with Technetium-99m. Sulfur colloid is used for liver, spleen and bone marrow scanning. Pertechnetate (TcO_4^-) behaves like iodine and is used in thyroid, salivary gland and stomach imaging. Methylene diphosphate (MDP) is used for bone scanning. One of the newest drugs is Hexamethylene Propyleneamine Oxime (HmPAO), which can cross the blood brain barrier and can be used to image blood perfusion in the brain.

Another radionuclide, indium-111, with a 67.1 hour half life and gamma rays at 247keV and 173keV, is used in labeling monoclonal antibodies. These antibodies are used for tumor scanning.

Other commonly used radionuclides in nuclear medicine include thallium-201, gallium-67, iodine-123, iodine-131, and Xenon-133.

Chapter II Anger Scintillation Camera

2.1 General

All nuclides used in nuclear medicine imaging emit gamma rays. A nuclear medicine image is a map of the distribution of the radionuclide emitting these gamma rays. A special camera must be used to form these images. Originally developed by H. O. Anger in 1958, this camera is referred to as a gamma camera, Anger scintillation camera, or simply an Anger camera. The basic concepts and operational characteristics of this camera will be described later in this chapter. First, however, the parameters used to characterize a camera system will be introduced.

2.2 Camera Parameters

The performance of a camera can be described in terms of several factors. The first parameter is resolution. There are three aspects to resolution: spatial resolution, energy resolution, and temporal resolution. Spatial resolution is a measure of the camera's ability to resolve spatially separated radioactive sources. Energy resolution is a measure of the ability of a camera to distinguish between gamma sources of different energies. Temporal resolution is a measure of the amount of time needed between two events for the camera to record the two events as separate events.

Another parameter is spatial linearity. Spatial linearity is a

measure of the accuracy of the positioning of events. It is used to characterize the amount of distortion or displacement inherent in a camera system.

The next parameter that will be considered is sensitivity. Sensitivity is a measure of the efficiency of a camera. It describes the number of counts detected per unit of source radioactivity. In a real camera, sensitivity can vary at different points within the camera's field of view.

Spatial uniformity is a measure of the ability of a camera to reproduce a uniform radioactive distribution. Non-uniform sensitivity and spatial non-linearities will contribute to spatial non-uniformities. If spatial non-linearities exist, some of the gamma rays will be misplaced in the image. Places where the events should have been recorded will register a lower number of events and conversely, places to where the events were misplaced, will record a higher number of events.

The parts of the camera and the effect of each part on the parameters above will be studied in the next section.

2.3 Parts of an Anger Camera

Figure 2.1 illustrates the basic parts of the Anger camera. The basic Anger camera consists of a lead collimator, a thin large diameter (about 40cm) scintillation crystal, an optional light pipe, photomultiplier tubes, amplifiers, and an electrical weighting network to determine the position and energy of scintillation events.

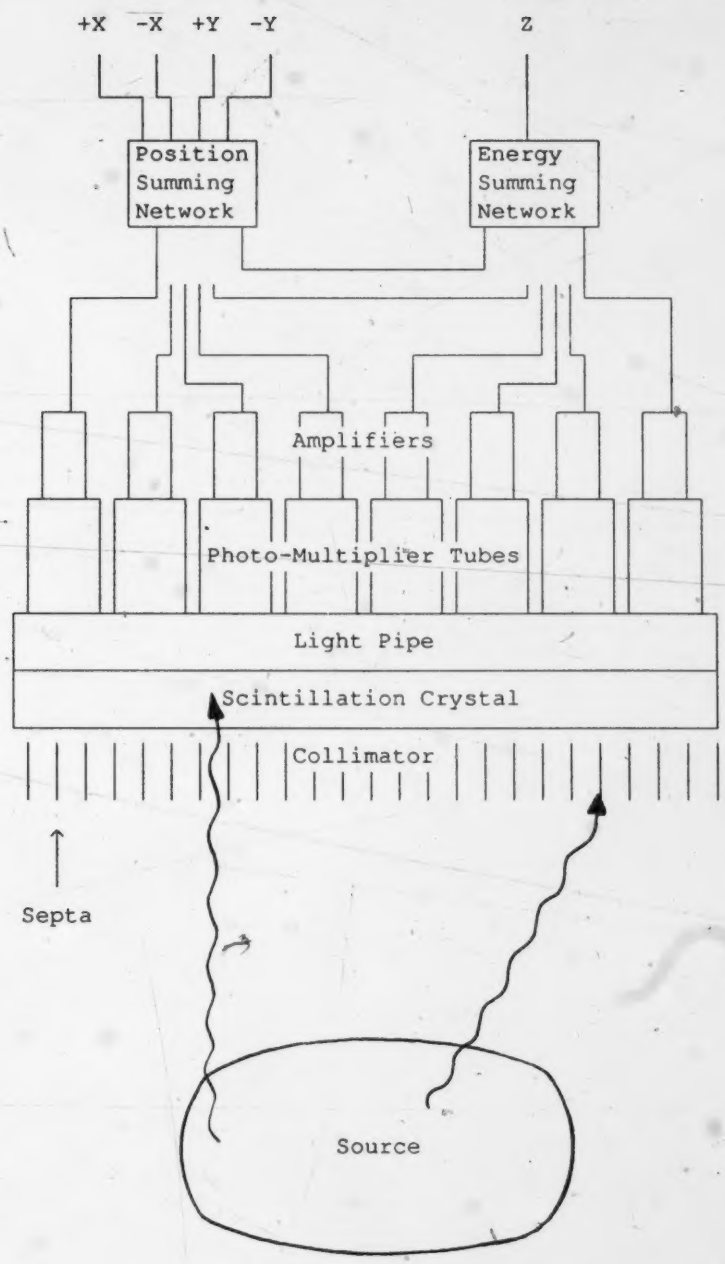

Figure 2.1 Block Diagram of an Anger Scintillation Camera

A lead collimator restricts the angle of incidence of incoming photons. After the photons have passed through the collimator, they can interact with the scintillation crystal and give off flashes of blue light. This scintillation light is collected by the light pipe and transmitted to the photomultiplier (PM) tubes. The PM tubes are arranged in a hexagonal configuration. The amplifiers increase the magnitude of the PM tubes' output pulses. They are connected to a positioning network and a summing network. The positioning network generates an X and a Y co-ordinate corresponding to the position of the scintillation in the crystal and the summing network creates a pulse proportional to the energy of the incident photon. The Z (energy) signal is fed into a pulse height analyzer which selects only photons within a pre-selected energy range. A detailed description of the individual parts follows.

2.3.1 Collimator

A parallel hole collimator is a piece of lead, about 1cm to 1.5cm thick, with holes perpendicular to its face. A cross section of a collimator is shown in figure 2.2. Lead foil or cast collimators are routinely used. The lead that separates the holes is called septa. The angle of acceptance can be approximated for small angles by equation 2.1:

$$\text{Angle of Acceptance} = \alpha = 2 \cdot \tan^{-1}\left(\frac{d}{2L}\right) \simeq \frac{d}{L} \quad \text{for } d \ll L \qquad (2.1)$$

The resolution of the collimator will depend on the acceptance angle and the distance from the source to the camera. As the source to camera distance, F, increases, the resolution decreases. As the holes

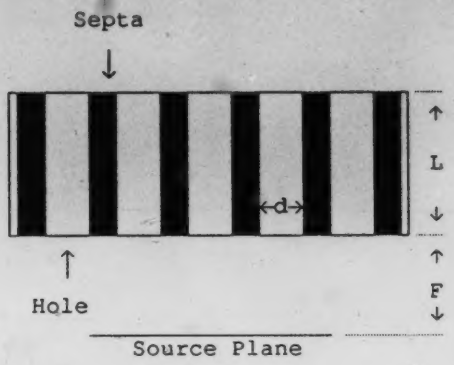

Figure 2.2 Parallel hole Collimator

get longer, the angle of acceptance gets smaller and hence, the blurring effect gets smaller. High resolution collimators have longer, narrower holes to improve the resolution. Unfortunately, as the angle of acceptance decreases, the number of photons that are accepted decreases. Therefore there is a trade off between angular acceptance and the sensitivity. In terms of camera performance, spatial resolution is traded for sensitivity.

Equation 2.1 neglects the possibility of gamma photons passing through the collimator's lead septa. At low energies this is a reasonable assumption. At higher energies, above 150keV, septal penetration becomes a problem. For clinical use, several collimators exist for different energies. For higher energy nuclides, such as Indium-111, a collimator with thick septa is used. For Technetium-99m, the collimator's septa are typically 0.5mm thick and the holes are 2.5mm in diameter. The septa in the collimator used with indium-111 are 1.5mm thick with 3.5mm diameter holes. To compensate for the loss of sensitivity when the septa are made

thicker, the holes are made larger. The result of switching to a higher energy collimator is thus a loss in spatial resolution of the camera.

In a real collimator, in order to maximize the number of holes, and hence the sensitivity, the holes are arranged in a hexagonal pattern and the holes may be hexagonal in shape. The effect of septal penetration on a point source with this type of collimator is a hexagonal star artifact due to the anisotropy of the septal thickness. This response must be considered only if a lot of septal penetration occurs.

2.3.2 Scintillation Crystal

Of the photons that pass through the collimator, some will interact with the scintillation crystal. A thallium doped sodium iodide crystal (NaI(Tl)) is very efficient at the energy range of interest to nuclear medicine. It has a half value thickness of about 3mm for 150keV photons and 11mm for 300keV photons. The thickness of a typical gamma camera scintillation crystal can vary from 6.4mm to 12.7mm. If the crystal is made thicker, the probability of interaction increases and the sensitivity of the crystal improves.

The NaI(Tl) scintillation crystal emits visible photons (λ_m=410nm) when it interacts with a gamma ray. The number of visible photons emitted varies with Poisson statistics but the average number of photons produced is proportional to the energy of the incoming gamma photon. When the gamma energy increases, more visible photons are emitted for each gamma ray interaction and the relative Poisson variation in the number of visible photons decreases.

The sodium iodide crystal is hygroscopic and must be hermetically sealed to prevent damage.

2.3.3 Light Pipe

When an interaction does occur, the light produced by scintillation is transmitted to the photomultiplier tubes by the light pipe. The light pipe optimizes the transmission of light from the crystal to the photomultiplier tubes by matching the index of refraction of the crystal to the PM tubes' glass entrance window. The light pipe also hermetically seals one side of the sodium iodide crystal.

2.3.4 Photomultiplier Tubes

The photomultiplier tubes convert the visible photons into a current proportional to the number of incident visible photons. The photomultiplier tubes are usually arranged in a hexagonal close packed configuration. A 40cm diameter camera can contain from 37 to 75 photomultiplier tubes. All the photomultiplier tubes will "see" each scintillation event. The amount of light that each tube receives will depend on the location of the scintillation event and the thicknesses of the NaI(Tl) crystal and the light pipe. The response of the photomultiplier tubes also varies statistically, because the number of electrons ejected at the photocathode in each photomultiplier tube varies from event to event. The sensitivity of the PM tubes also depends on where the photons strike the photocathode and on the presence of imperfections in the glass window.

Another source of variation in the output of the PM tubes is

instability in the high voltage applied to the PM tubes. A change of 1% in the applied high voltage can yield an output change of up to 10%. The result of these variations is a decrease in the energy resolution of the camera. Variations between tubes can cause differences in the energy response of the camera depending on the position of the scintillation event, which will contribute to spatial non-uniformity. Each PM tube must be individually tuned and matched to the rest of the tubes.

The PM tubes are also sensitive to temperature changes and magnetic fields. Proper shielding from the earth's magnetic field is very important for rotating gamma camera tomographic systems because the sensitivity of the camera must not change as the camera moves around the patient.

2.3.5 Amplifiers and Electrical Weighting Network

The output signals from the PM tubes are relatively small, and pre-amplifiers are used to magnify the signals. A weighting network, using a network of resistors, for example, is used to combine the signals from all the amplifiers so as to produce voltage signals proportional to the two dimensional location (X,Y) of the scintillation event. A summed voltage signal (Z) from all the photomultipliers, proportional to the energy of the incident gamma ray, is also obtained.

For a monoenergetic gamma ray source, the statistical variation in the scintillation crystal response, convolved with the variation in the PM tube response, results in a considerable broadening of the energy spectrum seen by the camera. The typical energy resolution for

140keV gamma rays is about 12% full width at half maximum (FWHM).

Energy spectra acquired with a General Electric camera are shown in figures 2.3 and 2.4. The FWHM of the technetium photopeak is about 16keV.

As was stated above, all the PM tubes see part of every scintillation event and the position of this event is determined from the relative magnitudes of the outputs of the PM tubes. The statistical variations in the number of scintillation photons and the variations in response of each PM tube will cause some misplacement of the position of a scintillation, thus degrading spatial resolution. As the crystal and/or light pipe thickness increases, the scintillation photons are spread over more PM tubes, with the result that spatial resolution is further degraded.

2.3.5.1 Temporal Resolution and Detector Saturation

The temporal resolution of the camera is affected by several factors. The scintillation light takes a finite amount of time to decay away, typically 230 nsec [So87], and the photomultiplier tubes and the amplifiers need approximately 0.6 msec [An84] to recover. If two photons interact with the crystal within a short time of each other, one cannot differentiate between the two interactions and they will appear to be one interaction. If the count rate is too high, pulse pile-up may occur in the electronics, degrading the image quality because of the increased probability of recording invalid events. Pulse pile up causes pulses from separate events to be summed. Since only pulses smaller than a certain size are accepted by the pulse height analyzer, the efficiency of the camera decreases

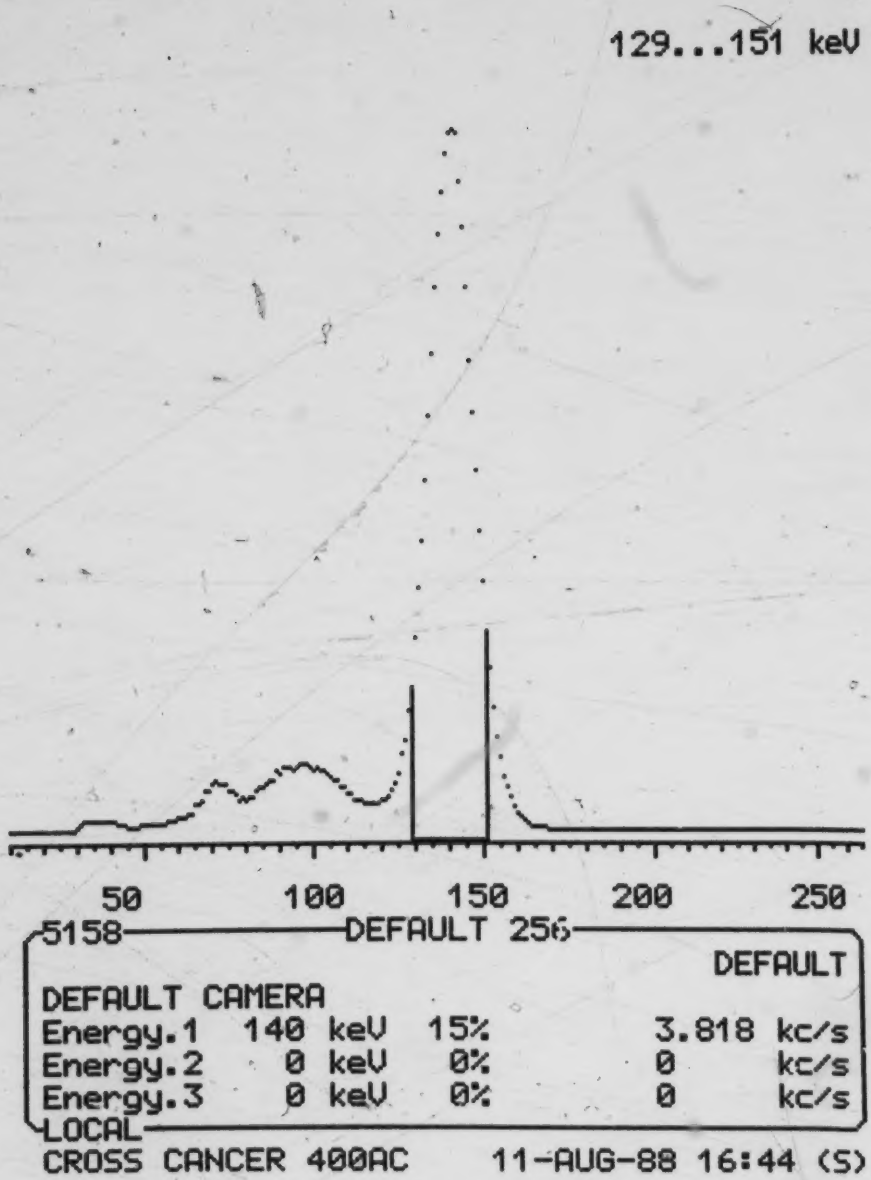

Figure 2.3 Technetium-99m spectrum from GE camera

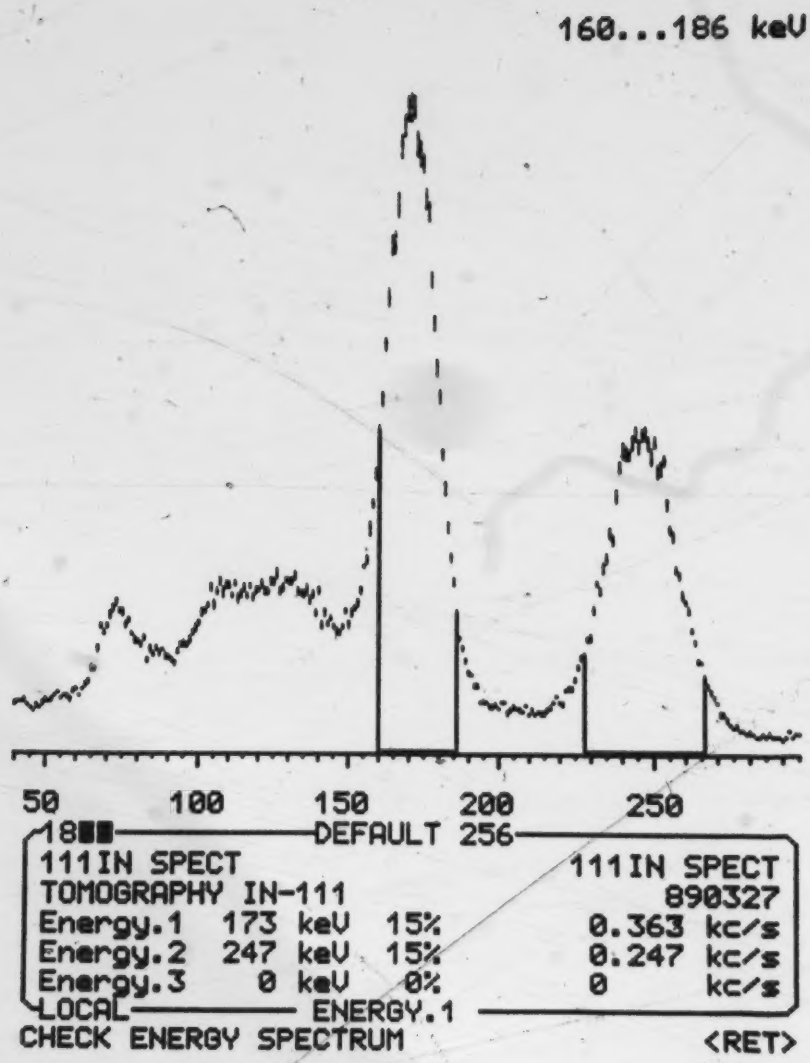

Figure 2.4 Indium-111 spectrum from GE camera

because valid events are lost or rejected by the electronics. For a typical Anger camera, a count rate of 75,000 counts per second yields a 20% decrease in expected count rate. In most clinical situations, count rates rarely exceed 20,000 counts per second.

2.3.6 Computer Interface

The camera, as described above, can be used with an analog display device and a pulse height analyzer to generate images. For many applications, however, images are acquired by a digital computer for display and further analysis.

As described earlier, the Anger camera produces X and Y positional signals. These signals must be digitized before the computer can use them. Digitization is performed by a specific piece of hardware called an analog to digital converter (A/D or ADC). The ADC's convert a voltage into an integer, binary number. A typical nuclear medicine camera has a twelve bit ADC. This means that a voltage is converted into a binary number between 0 and 4095 ($2^{12}-1$).

The smallest element of an image is called a pixel. Each pixel can be mapped back to a position on the scintillation crystal. In a nuclear medicine image, each pixel in the image contains the sum of the number of photons that interacted in a corresponding volume in the crystal. If a "hot" spot smaller than the dimension of a pixel is imaged, its intensity will be averaged over the area of the pixel. Images acquired clinically are typically 64 by 64, 128 by 128 or 256 by 256 pixels in size. Thus, only the most significant six, seven or eight bits of the ADC are used to determine the position (X and Y) of an event; the fractional part of the analog to digital conversion is

truncated.

2.4 Photoelectric Absorption and Compton Scatter

When high energy photons travel through matter they can interact with matter in a variety of ways. For photons with energies ranging from 100 to 500keV, the significant interaction mechanisms are photoelectric absorption and Compton scattering.

When a photoelectric interaction occurs, the high energy photon is totally absorbed by an atom. As a result, an orbital electron is ejected with an energy equal to the incident photon's energy less the binding energy of the electron. The electron dissipates its kinetic energy primarily by ionizing other atoms. It is the electrons that are ultimately responsible for the deposition of energy within matter.

When a photon collides with a loosely bound electron, Compton scatter may occur. The photon loses some energy as it scatters, and the energy lost by the photon is converted into kinetic energy of the electron. Figure 2.5 illustrates the process.

The relationship between the angle of scatter, the scattered photon's energy and the electron's kinetic energy is given by equation 2.2. [At86]

$$E' = \frac{E_0}{1 + \frac{E_0}{m_0 c^2}(1 - \cos\Theta)} \qquad (2.2)$$

In order to prevent accepting photons that have been scattered,

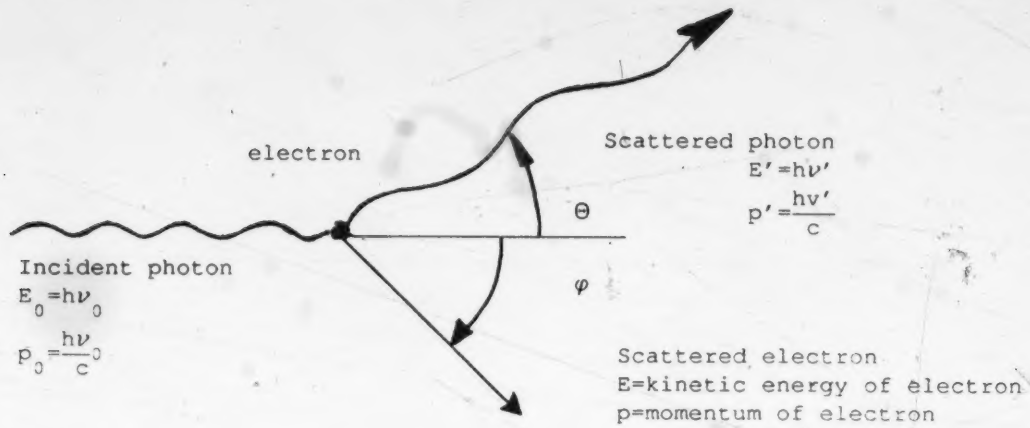

Figure 2.5 Compton Scattering

only photons with energy greater than a lower limit are accepted. Photons with energy above a certain upper limit are also rejected because of pulse pile up. This leaves a window of acceptable energy. An energy window for an Anger camera is typically 15% of the photon energy.

Photons emitted towards the detector may not reach the detector for two reasons. In the intervening material between the camera and the radioactive source, a photon may be photoelectrically absorbed or Compton scattered away from the detector. This is referred to as attenuation and for a collimated system can be approximated by equation 2.3.

$$A = A_0 e^{-\mu x} \tag{2.3}$$

where A = flux of photons reaching camera

A_0 = flux of photons emitted toward detector

μ = linear attenuation coefficient

x = thickness of material between emitter and detector

For 140keV photons passing through water, $\mu = 0.15cm^{-1}$ and for 247keV photons, $\mu = 0.13cm^{-1}$.

It is also possible for a photon emitted in a direction not directly towards the detector to be scattered toward the detector. Although the scattered photon has less energy, the poor energy resolution of the Anger camera does not permit the discrimination of many of these scattered photons from unscattered photons. For example, for an Anger camera operating with an energy window centred at 140keV and having a width of 15% (i.e. 21keV), a photon would have to be scattered by over 45° before it would fall outside the energy window.

Chapter III SPECT

3.1 Definition and Description of SPECT

By taking several two dimensional images, with the Anger camera discussed in chapter II, from various angles around a subject, a three dimensional image can be reconstructed using tomographic techniques. This technique in nuclear medicine is called rotating gamma camera Single Photon Emission Computed Tomography or SPECT.

SPECT has two main advantages over planar imaging. Since the target organ can be separated (mathematically) from the background, by removing the overlying and underlying activity, the contrast of the images is significantly improved over planar images [Co86]. Furthermore, SPECT provides a complete three dimensional visualization of the organ or structure of interest.

The main disadvantages of rotating gamma camera SPECT are as follows. Spatial resolution is often poor because the rotating gamma camera cannot be positioned as close to the patient as in planar imaging. Any noise inherent in the original "projection" images is amplified by the reconstruction process. The time required to acquire a complete set of "projection" images can vary from twenty to sixty minutes, during which time the distribution of the radiotracer within the patient must not change, and the patient must not move. These time constraints limit, to some extent, the radiopharmaceutical and the category of the patient to be imaged.

3.2 Reconstruction Mathematics

In this section, the mathematics of parallel ray tomography will be introduced. The equations and results will be presented without derivation or proof. For a more complete discussion of reconstruction mathematics, the reader is referred to references [Du84] and [Ka88].

Figure 3.1 defines the co-ordinate systems to be used for the equations. The gamma camera rotates around the patient, about an axis of rotation, z, perpendicular to u_1 and u_2. The axis v_1 is parallel to the camera face and perpendicular to the camera's axis of rotation and v_2 is a direction normal to the camera face.

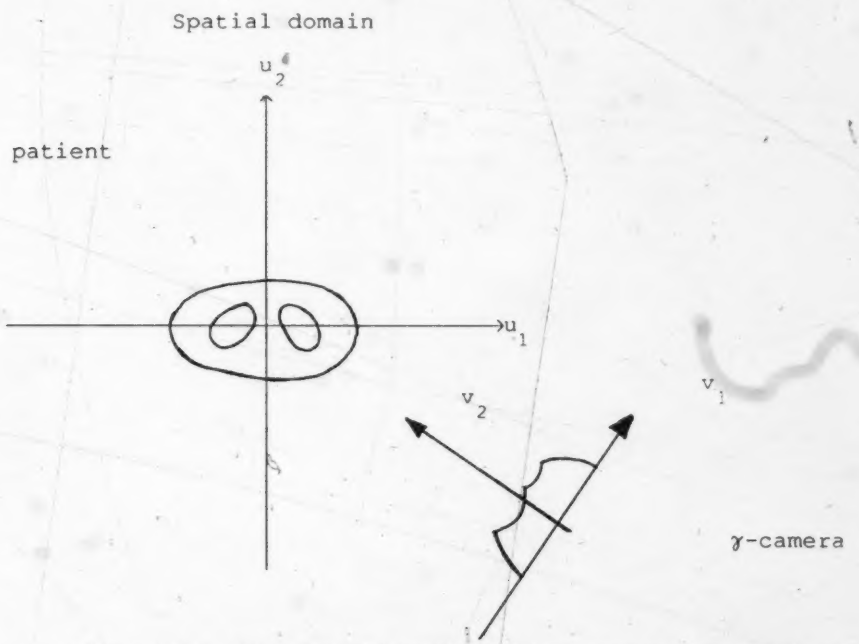

Figure 3.1 The Relationship of the camera and patient co-ordinate systems

The Anger camera "sees" a two dimensional projection of a three dimensional object. Each point in the projection image is made up of

the sum of all the activity along a line normal to the camera face. For the purpose of discussion, assume the three dimensional object is made up of a series of two dimensional slices. The one dimensional projection of a two dimensional slice is described by equation 3.1

$$p_\Theta(v_1) = \int_{-\infty}^{\infty} x\ (u_1, u_2)\ dv_2 \qquad (3.1)$$

where $x\ (u_1, u_2)$ is the two dimensional slice of an object.

As long as the object is finite in extent, the limits of integration do not have to go all the way to infinity because the activity will go to zero outside the object.

The next equation to consider is the Fourier Slice theorem, illustrated in figure 3.2. For an n+1 dimensional object with an n-dimensional projection, the Fourier Slice theorem states that the n-dimensional Fourier transform of a projection of an object is equal to the (n+1)-dimensional Fourier transform of the object evaluated along the plane parallel to the projection plane. Equation 3.2 expresses this statement mathematically.

$$\mathcal{F}\left\{ p_\Theta(v_1) \right\} = S_\Theta(\omega) = X\ (\ \Omega_1 = \omega \cos\Theta\ ,\ \Omega_2 = \omega \sin\Theta\ ) \qquad (3.2)$$

where

$S_\Theta(\omega)$ is the one dimensional Fourier transform of the projection at an angle Θ given by equation 3.3.

$$S_\Theta(\omega) = \mathcal{F}\left\{ p_\Theta(v_1) \right\} = \int_{-\infty}^{\infty} p_\Theta(v_1) \cdot e^{-j\omega v_1}\, dv_1 \qquad (3.3)$$

where ω represents the spatial frequency

$X\ (\Omega_1=\omega\cos\theta\ ,\ \Omega_2=\omega\sin\theta\ )$ is the two dimensional Fourier transform of the two dimensional object $x\ (u_1,u_2)$ evaluated along the line $(\ \Omega_1=\omega\cos\theta\ ,\ \Omega_2=\omega\sin\theta\ )$

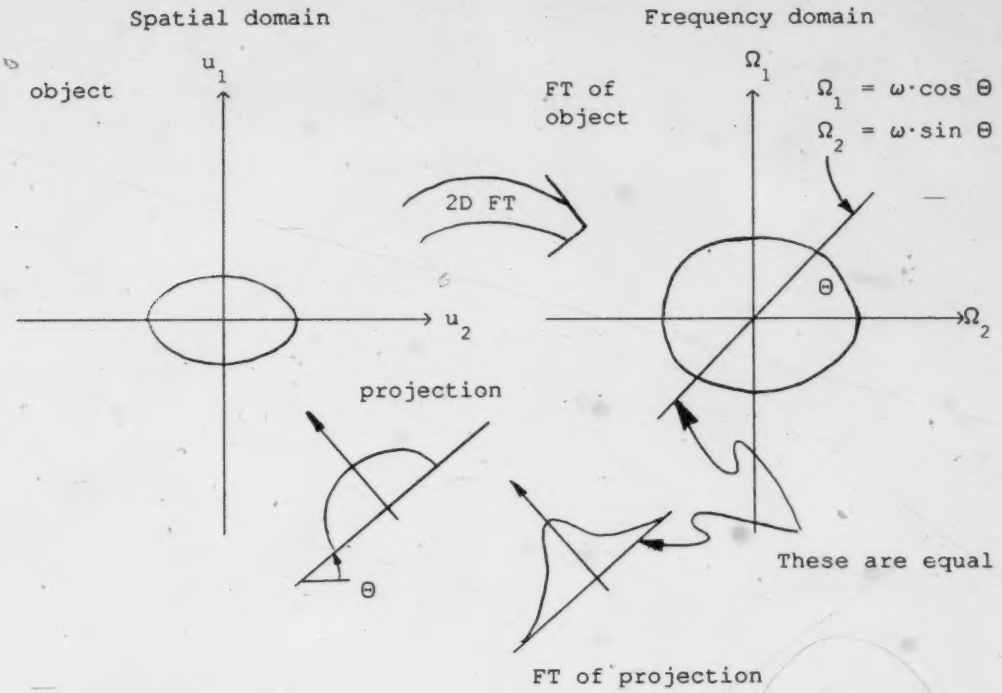

Figure 3.2 Co-ordinate system used to describe Fourier Slice theorem

If there are enough projections, the Fourier transform of the object can be reconstructed. The object, $x\ (u_1,u_2)$, can then be calculated from the transform. Equation 3.4, called the Radon inversion formula, reconstructs the object from the projection data

$$x\ (u_1,u_2) = \frac{1}{2\pi}\int_0^{\pi} \mathcal{F}^{-1}\left\{ S_\theta(\omega)\ \cdot\ |\omega| \right\} d\theta \qquad (3.4)$$

where $|\omega|$ is a ramp or back projection filter, and $S_\theta(\omega)$ is

the Fourier transform of the projection given by equation 3.3.

Calculating the object, $x(u_1,u_2)$, in this manner is called filtered backprojection because the ramp filter is applied in the frequency domain. Alternately, the processing could have been performed in the spatial domain. The spatial domain equation is given by equation 3.5.

$$x(u_1,u_2) = \frac{1}{2\pi} \int_0^{\pi} \left[p_\Theta(v_1) * k(v_1) \right] d\Theta \qquad (3.5)$$

where $*$ represents a convolution operation

and $$k(v_1) = \mathcal{F}^{-1}\left\{ |\omega| \right\} = \text{Radon kernel} \qquad (3.6)$$

Performing convolution backprojection has some advantages. The filtering kernel, $k(v_1)$, may be modified as a function of space. Non shift invariant systems may be handled by this method. However, this is beyond the scope of this thesis.

Although the mathematics of tomographic reconstruction is exact, problems in reconstruction occur due to limitations of the projection images. Noise, spatial resolution, digitization, and the finite number of projection images contribute to the degradation of the reconstructed images. As the quality of the projection images improves, the reconstructed images will also improve.

The filtered backprojection method is used to reconstruct tomographic images. In addition to the ramp filter, other filters can be used to improve the quality of the projection images. For example, filters to suppress noise and to enhance spatial resolution can be implemented with the backprojection (ramp) filter.

Chapter IV Image Processing in the Fourier Domain (Filtering)

4.1 System Response and Image Characteristics

As seen in chapter II, there are various reasons why a photon entering and interacting in the detector can be misplaced. When many photons are collected, these misplaced photons tend to blur an image. This blurring determines the system spatial resolution.

One way to measure the system resolution is to place a small source of activity in front of the camera and to observe the image. If the camera was ideal, the image would be a point. However, the camera is not ideal and the point gets "spread" out. The response of the camera to a point source is called the point spread function (PSF) or the impulse response of a system. The point spread function often has a Gaussian shape. The full width at half maximum (FWHM) of the point spread function is one measure of the spatial resolution of the system.

If the response of the system is independent of the x and y position of the point source, the system is said to be shift invariant. For nuclear medicine imaging, it is reasonable to assume linearity and shift invariance, since the non-linearities and the spatial dependence are small enough to ignore. If the two conditions of linearity and shift invariance hold, then Fourier transform techniques can be used for tomographic reconstruction and image processing.

4.2 Fourier Techniques

There are computational advantages to working in the frequency domain. The Fast Fourier Transform (FFT) is an efficient way to transform a finite sized set of discrete data. The Radon inversion technique uses the Fourier transform when the backprojection filter is applied to a projection, and a resolution recovery or noise suppression filter can be added with little additional computer overhead.

Figure 4.1 shows a generalized imaging system. Mathematically, a system maps an input function, $x(u_1,u_2)$, into an output function, $y(u_1,u_2)$. The mapping can be expressed by an operator. If only linear shift invariant operators are considered, the operator can be uniquely characterized by a convolution operation with a point spread function, $h(u_1,u_2)$.

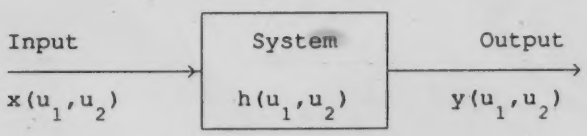

Figure 4.1 Response of System

It is generally assumed that the PSF is radially symmetric and as a result, its two dimensional Fourier transform is also radially symmetric. The Modulation Transfer Function or MTF is simply the absolute value of the Fourier transform of the PSF collapsed to one dimension. The PSF of an ideal system is a single point. The Fourier transform of a point is a flat spectrum, and thus an ideal system

would have a flat frequency response for all frequencies.

If a delta function or point source is imaged with the system shown in Figure 4.1, the output response, $y(u_1,u_2)$, obtained is equal to the PSF, $h(u_1,u_2)$. If the same situation is considered in the Fourier domain, when an object with a flat spectrum is imaged, the MTF can be obtained by collapsing the Fourier transform of the output to one dimension. A transfer function is defined as the transform of the output divided by the transform of the input function. Since the transform of a delta function is a constant, the transfer function can be found by taking the Fourier transform of the point spread function.

For any arbitrary input function, $x(u_1,u_2)$, with an output function, $y(u_1,u_2)$, and the Fourier transform operator is denoted by $\mathcal{F}\{\ \}$

if $$\mathcal{F}\left\{ x(u_1,u_2) \right\} = X(n_1, n_2) \quad \text{and} \tag{4.1}$$

$$\mathcal{F}\left\{ y(u_1,u_2) \right\} = Y(n_1, n_2) \quad \text{then} \tag{4.2}$$

$$\text{Transfer Function} = H(n_1, n_2) = \frac{Y(n_1,n_2)}{X(n_1,n_2)} \tag{4.3}$$

To find the output to an arbitrary input function, the transform of the input function is multiplied by the transfer function and the result is inverse transformed as shown in equations 4.4 and 4.5.

$$\mathcal{F}\left\{ y(n_1,n_2) \right\} = \mathcal{F}\left\{ x(n_1,n_2) \right\} \cdot H(n_1,n_2) \tag{4.4}$$

or in the spatial domain,

$$y(n_1,n_2) = \mathcal{F}^{-1}\left\{ \mathcal{F}\left\{ x(n_1,n_2) \right\} \cdot H(n_1,n_2) \right\} \tag{4.5}$$

The use of transform methods to describe systems is analogous to

multiplying numbers by adding their logarithms. A transform operation and a simple multiplication operation replace a more time consuming convolution operation.

The point spread function of a real system has roughly a Gaussian shape. The Fourier transform of a Gaussian with a width, σ, is another Gaussian with width, $\frac{1}{\sigma}$, as can be seen in equation 4.6.

$$\mathcal{F}\left\{ e^{\frac{-t^2}{2\sigma^2}} \right\} = \sigma\sqrt{2\pi}\, e^{\frac{-\sigma^2\omega^2}{2}} \qquad (4.6)$$

The width of the transform is inversely proportional to the width of the original function.

All the derivations of the mathematics used for tomography have been done for the continuous case. With digital computers, only discrete data can be handled and therefore a few words must be said about sampled data.

The Nyquist theorem states that in order to be able to faithfully reproduce an input signal, the input signal must be sampled at a rate at least twice as high as its highest spatial frequency component. This means that, if a spatial resolution of r is desired, then the sampling interval must be smaller than r/2. Objects sampled at a finite number of points must therefore have a limited bandwidth. Because of the physical limitations of the imaging system, the gamma camera acts like an analog low pass filter and limits the bandwidth of the signal before it reaches the computer where the signals are sampled.

For practical reasons, only a finite number of projection images

can be acquired. The Nyquist theorem is also used to determine how many projection images are required for a tomographic reconstruction. Clinically, with 64 by 64 pixel planar images, 64 projection images are acquired.

4.3 Image Characteristics

Images may be characterized by three parameters: noise, contrast, and spatial resolution.

Noise is defined as random fluctuations present in physical processes that tend to obscure or mask the desired signal or image. Noise may be random or deterministic. For image processing in nuclear medicine, noise is usually modelled as being random. Noise will be considered in more detail in section 4.4.

Contrast is a measure of the signal to background ratio as illustrated in figure 4.2. Contrast can be measured by imaging a phantom with hot spots and cold spots of known activity.

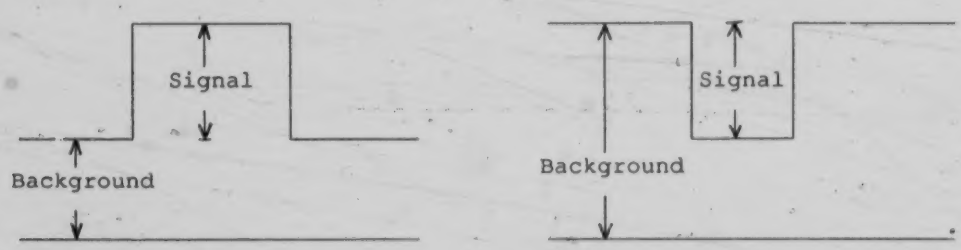

Figure 4.2 Contrast is measured as the signal to background ratio

As seen in chapter II, the collimator affects the camera's spatial resolution. The combined spatial resolution of the camera and the collimator is defined as the system resolution. Resolution is

usually measured in terms of the FWHM and the full width at tenth maximum (FWTM) of the point spread function. Figure 4.3 illustrates the point spread functions and the MTFs of the low energy general purpose (LEGP) collimator and the medium energy standard parallel (MESP) collimator. The spatial resolution of the camera is also affected by source to camera distance and the amount of scatter material between the source and the camera, as will be discussed later.

4.4 Noise

Images are acquired by counting photons emitted through radioactive decay. With radioactive decay, the time between transitions varies statistically with Poisson characteristics around a mean value. This means that the number of atoms that decay per unit time cannot be measured exactly. The uncertainty in the number of decays is proportional to the square root of the number of photons measured. As the number of photons counted, N, increases, the fraction of uncertainty decreases, as illustrated in equation 4.11.

$$\text{Fraction of uncertainty} = \frac{\text{Uncertainty in count}}{\text{Total count}} = \frac{\sqrt{N}}{N} = \frac{1}{\sqrt{N}} \qquad (4.11)$$

To minimize noise, it is desirable to maximize the number of counts per pixel in an image. The count can be increased by increasing the imaging time. SPECT scans can take from thirty minutes

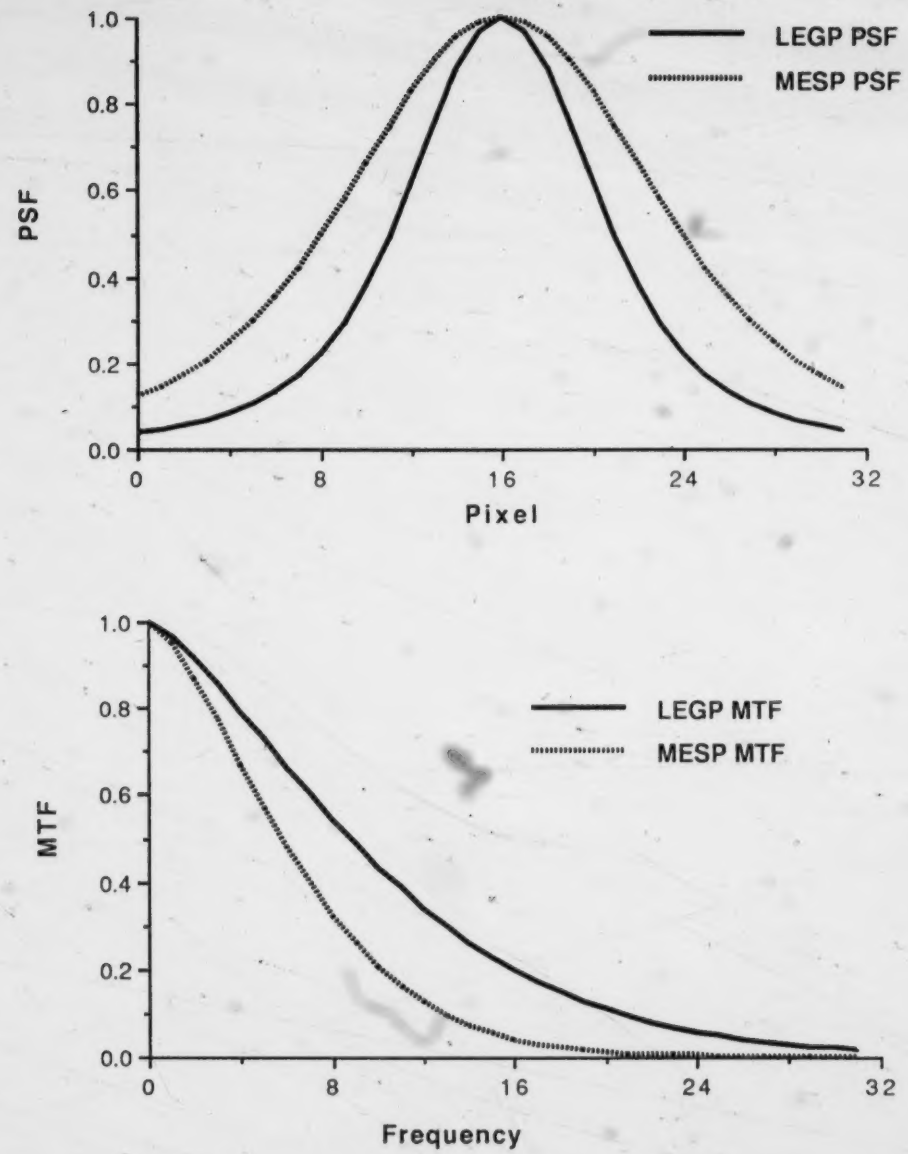

Figure 4.3 Point spread function and modulation transfer function for the LEGP and the MESP collimators.

to an hour to acquire.

4.5 Distance and Scatter

As seen in chapter II, as the distance from the source to the camera increases, the spatial resolution of the images decreases. As the amount of scatter material between the source and the camera increases, the resolution also becomes poorer. When scattering material is inserted the number of Compton scattered photons increases. As illustrated in figure 4.4, the FWHM of the point spread function increases slightly, but the FWTM increases significantly. In the Fourier domain, the low frequency components of the MTF will be boosted.

4.6 Filter Theory

Recall that the gamma camera's point spread function is approximately gaussian in shape. The MTF of the gamma camera will also be gaussian in shape. The frequency spectrum of an image will be the product of the MTF and the frequency spectrum of the object. The high frequency components in the object will be reduced by the MTF of the imaging system. If noise is considered in the Fourier domain, it has components at all frequencies. The image in the frequency domain is modelled by equation 4.12.

$$Y(U_1,U_2) = H(U_1,U_2) \cdot X(U_1,U_2) + N(U_1,U_2) \qquad (4.12)$$

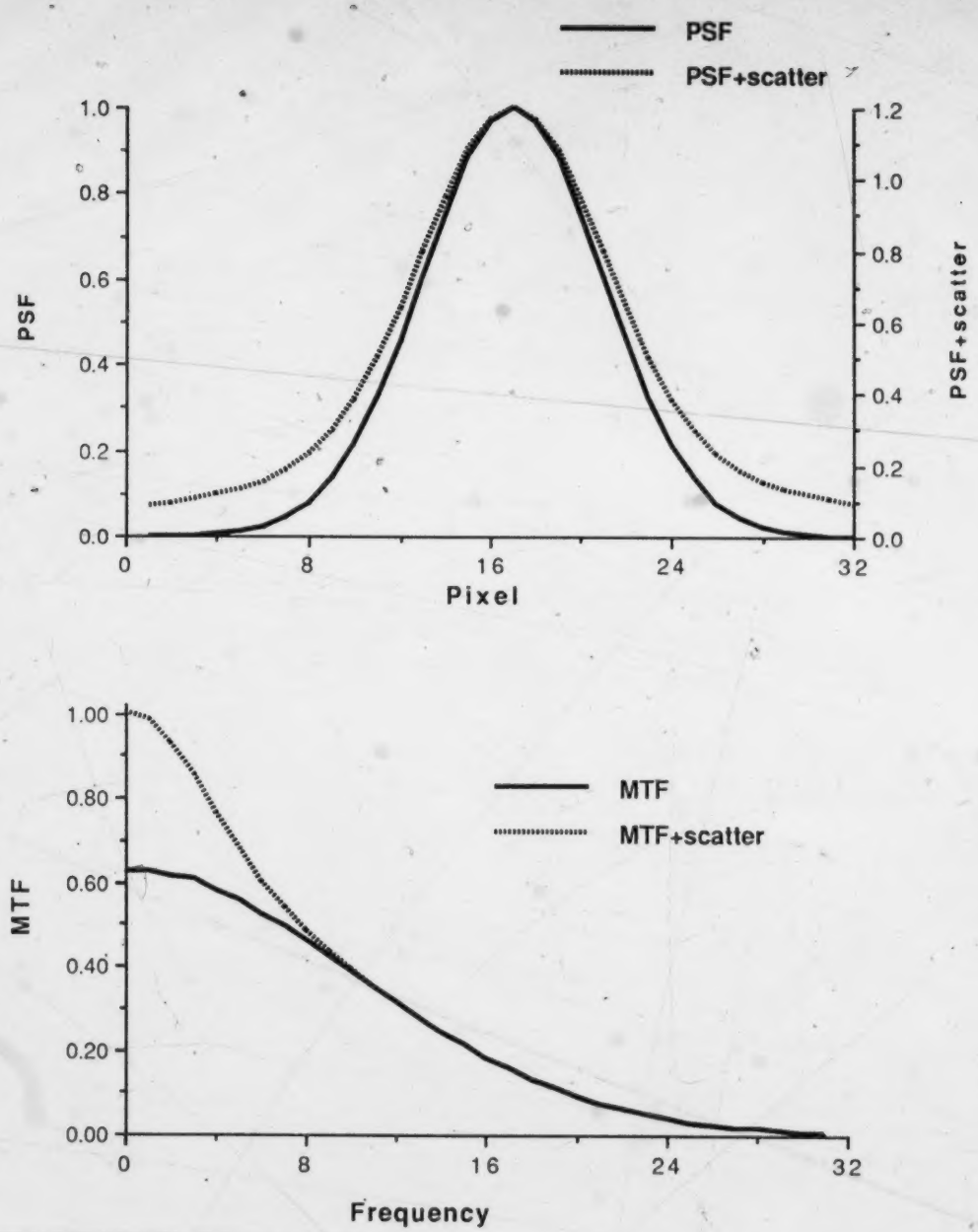

Figure 4.4 Effect of scatter material on the point spread function and the modulation transfer function.

where $Y(U_1,U_2)$ is the Fourier transform of the image

$X(U_1,U_2)$ is the Fourier transform of the object

$H(U_1,U_2)$ is the Fourier transform of the PSF

$N(U_1,U_2)$ is the Fourier transform of the noise

At low frequencies, the image's power spectrum will be dominated by the object's power spectrum. At high frequencies, the MTF of the system will reduce the frequency spectrum of the object and the frequency components of the noise will dominate.

A filter is a mathematical operator used to suppress or enhance information in different frequency ranges. It could be used to reduce the higher frequency components of the image where noise tends to dominate, and hence suppress the noise. This type of filter is a noise suppression low pass filter. One of the most commonly used low pass filters is the Butterworth filter, which will be described in the next section.

The MTF of the camera reduced the power spectrum of the object. If the frequency components that were suppressed by the camera are boosted by a filter, some of the resolution lost by the camera can be regained. This type of a filter is called an enhancement or resolution recovery filter because it enhances certain frequency components. The enhancement filter must be designed carefully in order to prevent the amplification of noise. An enhancement filter combined with a low pass filter, called a Metz filter, will also be described in the next section.

The ramp filter, used in the reconstruction of tomographic images, was introduced in the previous chapter. The gain of the ramp filter increases as frequency increases, and thus this filter

amplifies the high frequency noise in images. A second filter, such as the Butterworth or Metz, must almost always be used in conjunction with the ramp filter to suppress high frequency noise.

4.7 Actual Filters

Two filters implemented in the SPECT reconstruction program will be described in this section. One of the most commonly used low pass filters to limit high frequency noise is the Butterworth filter. In one dimension, its form is given by equation 4.13.

$$H(f) = \frac{1}{\left[1 + \left(\frac{f}{F_C} \right)^n \right]^{1/2}} \qquad (4.13)$$

where F_C = cutoff frequency

n = roll off parameter

f = frequency variable

For a two dimensional image, the response of the system is radially symmetric to first order, and therefore f can be replaced with the radial frequency.

For the tomographic reconstruction of liver scans, a Butterworth filter with a cut off frequency 0.48 times the Nyquist frequency and a roll off parameter of n=12.5 has previously been used. For a 64 by 64 pixel image the Nyquist frequency, F_N, is 32 pixels^{-1}.

The Butterworth filter used for liver scans is shown in figure 4.5. Notice that the filter starts to roll off at $0.48 \cdot F_N$.

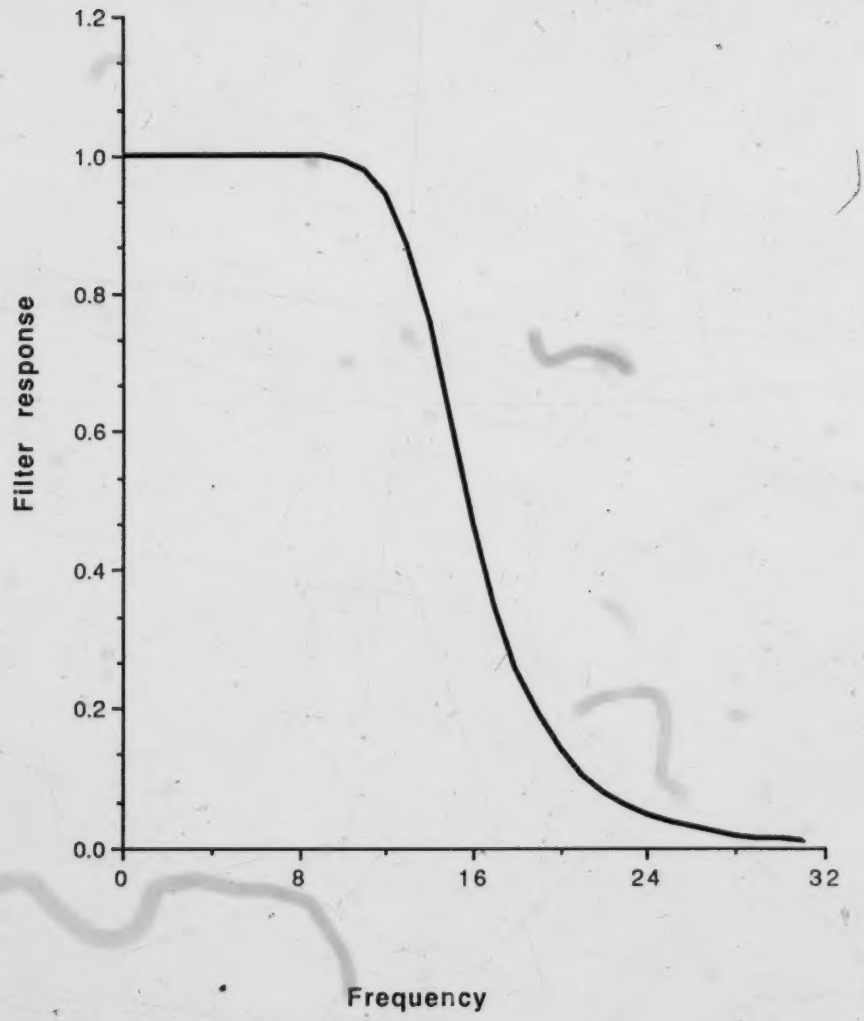

Figure 4.5 Butterworth filter with $F_C/F_N = 0.48$ and n=12.5

The Metz filter is an enhancement filter. In one dimension, its form is given by equation 4.14.

$$H(f) = MTF^{-1} \cdot \left[1 - (1 - MTF^{2}(f))^{X} \right] \qquad (4.14)$$

where MTF(f) = modulation transfer function

X = cutoff parameter

f = frequency variable

The Metz filter is plotted for various parameters in figure 4.6. From equation 4.14 it can be seen that, at low frequencies where the MTF has a value close to one, the Metz filter is essentially an enhancement filter. However, as the MTF approaches zero at high frequencies, the Metz filter rolls over to become a noise suppression filter. The location of the roll over is determined by the X parameter.

By changing the X parameter, the Metz filter can be adapted to the particular noise characteristics of an image to be filtered. King et al. [Ki87] have developed a procedure for calculating the "optimum" X parameter for an image. This technique is illustrated in figure 4.7, and is summarized by the following steps:

- The two dimensional power spectrum of the image to be filtered is calculated. The power spectrum of an image is defined as the square of the magnitude of the frequency components, i.e. in this case, the two-dimensional Fourier transform squared.
- The two dimensional power spectrum is collapsed to one dimension assuming radial symmetry.
- The flat, high frequency region of the power spectrum is dominated by noise. The X parameter is chosen to suppress this

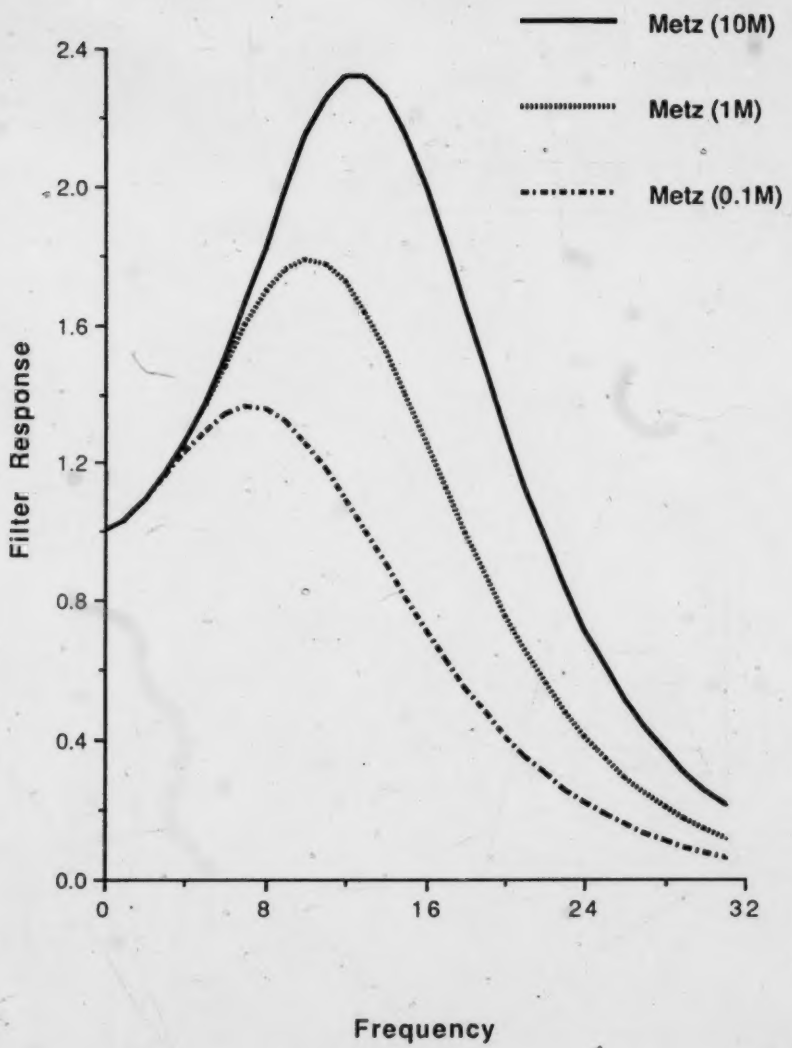

Figure 4.6 Metz filter implemented for various count images

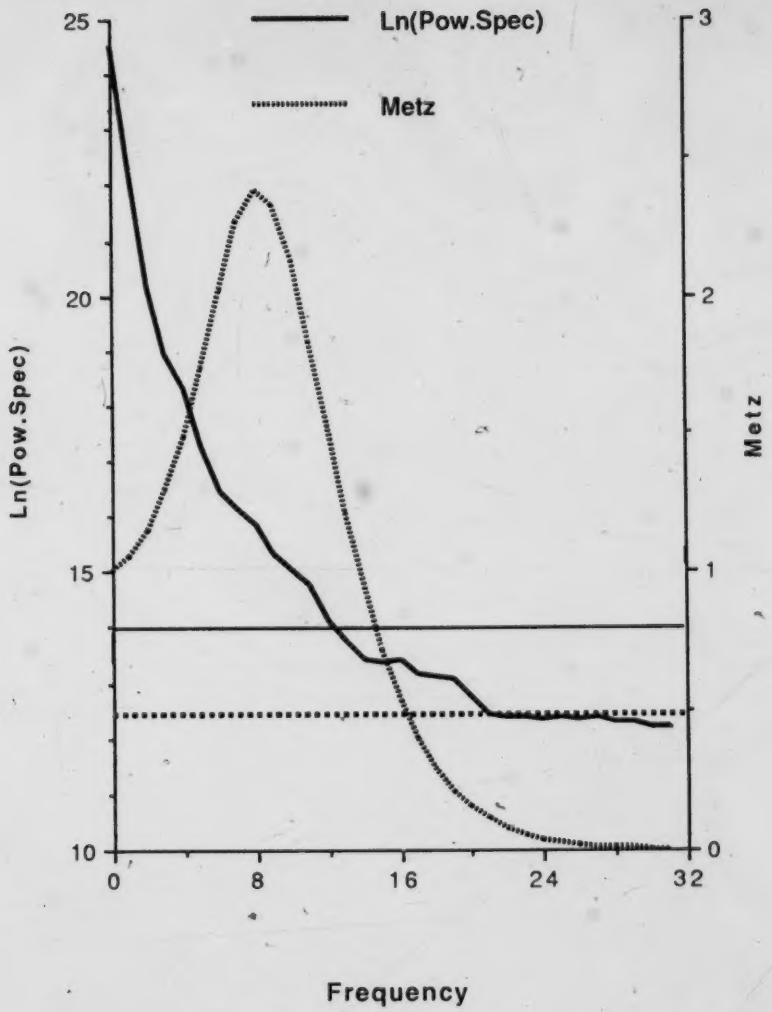

Figure 4.7 Log of an image's power spectrum used to determine the X parameter of an image dependent Metz filter.

noise by making the filter's gain equal to unity at a point where the power spectrum signal is 3.3 times greater than the background noise level. This power spectrum threshold is illustrated in figure 4.7 by the horizontal dashed line.

The expression for the MTF(f) in the filter should reflect the camera's MTF. Unfortunately, the MTF of the camera varies with imaging conditions such as the distance from the source to the camera and the amount of scattering material between the source and the detector.

The MTF(f) may be experimentally determined for clinically significant imaging conditions or it may be approximated by an analytic expression fitted to clinical imaging results. The MTF can be modelled by equation 4.15.

$$MTF(f) = e^{\left(- \frac{f^{P}}{S} \right)} \qquad (4.15)$$

The parameters P and S depend on the collimator used with the camera. For the low energy, general purpose (LEGP) collimator, P=1.4 and S=30. For the medium energy, special purpose (MESP) collimator P=1.5 and S=20.

The Butterworth and the Metz filters, described above, have been used clinically in the Nuclear Medicine Department of the Cross Cancer Institute. Their performance will be evaluated in the experiments discussed in the following chapter.

Chapter V Experiments

5.1 Objectives

As discussed in earlier chapters, a three dimensional SPECT data set is reconstructed from a series of two dimensional projection images acquired at various angles around a patient. It is assumed that by optimizing these projection images, the quality of the reconstructed tomographic images will improve.

As seen in section IV, the quality of an image can be studied in terms of three properties: noise, contrast and spatial resolution. These properties are affected by various imaging conditions, most noticeably the number of gamma rays detected, the distance between the radioisotope source and the gamma camera, the amount of scattering material between the source and the camera, the energies of the emitted gamma rays, and the characteristics of the camera collimator.

Several experiments were performed which involved the acquisition of test images under different imaging conditions. The objective of these experiments was to quantify the effects on image quality of both variations in imaging conditions, and of different image processing filters. Tests were performed to measure noise and contrast, and a test that compared a given image with a high quality, reference image was also devised.

5.2 Apparatus

The gamma camera system used to acquire images in the experiments was a General Electric 400A Starport system. The performance specifications for this camera are given in Appendix I. The specifications were measured according to industry standard (NEMA) guidelines [Ne86].

The computer used to acquire the images was a Picker PCS-512 (PDP 11/73) computer with an Analogic AP-400 array processor. A program called Gamma-11 was run on the computer to annotate, acquire and store images in a predefined file structure.

Because of limits in image resolution, clinical SPECT projection images are acquired in 64 by 64 pixel images. In order to simulate the clinical situation, the experiments were performed on 64 by 64 pixel images.

Since the computer and the camera were used clinically throughout the day, another computer, a VAX 11/750, was used to analyze experimental data. Gamma-11 image files were transferred from the PCS-512 system to the VAX using an Ethernet network.

Experimental image processing software was written on the VAX in VAX FORTRAN. This version of FORTRAN is very similar to the FORTRAN-77 used on the PCS-512 systems, and hence these programs could be converted to run on the PCS-512 system with only minor modifications.

To study the effect of noise on image quality, a flood tank phantom was used. The flood tank was a 40.0cm by 40.0cm by 5.5cm Plexiglas container, filled with water into which a radiotracer was

mixed. Care was taken to ensure that the tracer was uniformly distributed throughout the water; in particular, a pharmaceutical that did not adhere to the Plexiglas was chosen. For the low energy isotope, pertechnetate (TcO_4^-) was used because it is used in weekly quality control procedures and is known not to adhere to the Plexiglas.

However the medium energy radiotracer, ^{111}In-citrate, is not used for routine quality control procedures and preliminary experiments indicated that precipitation occurred. It was suggested that if the pH of the water in the phantom was decreased below about 3, the precipitation could be minimized†. This hypothesis was confirmed experimentally using a small test container. The pH of the water in the flood tank and in the test phantom, described below, was therefore decreased to 2.6 using acetic acid, in order to prevent the indium citrate from sticking or plating out on the Plexiglas.

To generate experimental planar images, a special contrast/resolution test phantom, hereafter referred to simply as the test phantom, was designed and constructed‡. This phantom consisted of a box, with inside dimensions of 29.8 cm by 34.9 cm by 4.1 cm, with various Plexiglas inserts. Figure 5.1 illustrates the structure of the the phantom. The Plexiglas inserts reduced the thickness of the water. Since the image acquired by the camera was a projection of the activity in the object, the activity imaged by the camera was, neglecting attenuation, proportional to the thickness of the water.

---

†The author wishes to thank Mr. Ron Schmidt and Ms. Candice Schwab for their help with the precipitation problem.

‡The author wishes to thank Mr. Finn Mortensen for his assistance designing and building the phantom.

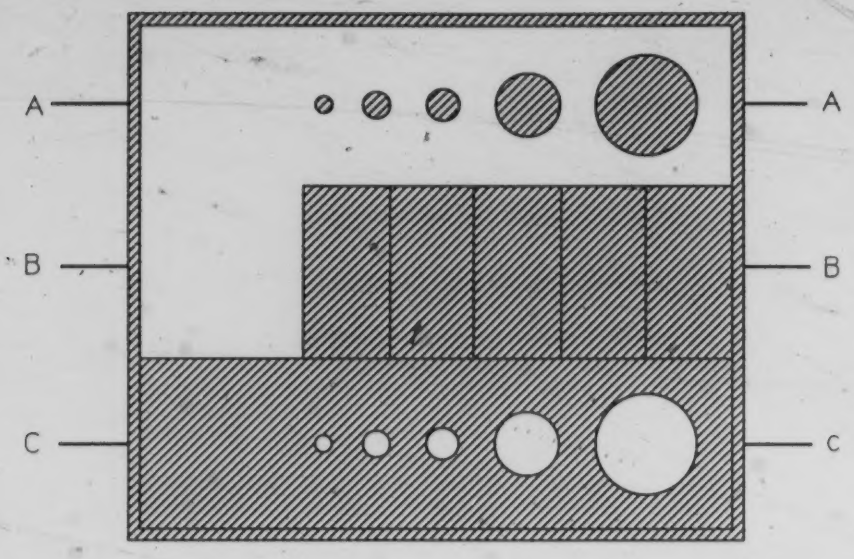

Section A-A

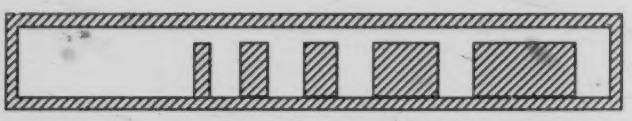

Section B-B

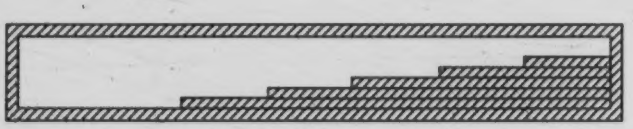

Section C-C

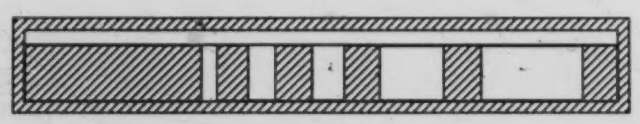

Figure 5.1 Top and cross sections of test phantom.

5.3 Procedure for the Acquisition of Images

5.3.1 Experiment I

Experiment I was performed using the low energy isotope, technetium-99m, with the Low Energy General Purpose (LEGP) collimator installed on the camera.

5.3.1.1 Part a

The objective of the first part of experiment I was to characterize the noise in various images and to observe the effect of filtering on the noise.

Technetium-99m pertechnetate was added to the flood tank. The flood tank was imaged on the collimator face. This was done to isolate the noise from other factors that degrade images, such as scatter and camera-to-phantom distance. Images with total counts of 10 thousand, 100 thousand, 1 million, 10 million, and 100 million were acquired. These values were chosen to bracket the range normally seen in clinical studies.

5.3.1.2 Part b

The objectives of the second part of experiment I were to observe the effect of varying count, varying distance, varying amounts of scattering material, and filters on image quality.

The experimental setup is shown in figure 5.2. To simulate

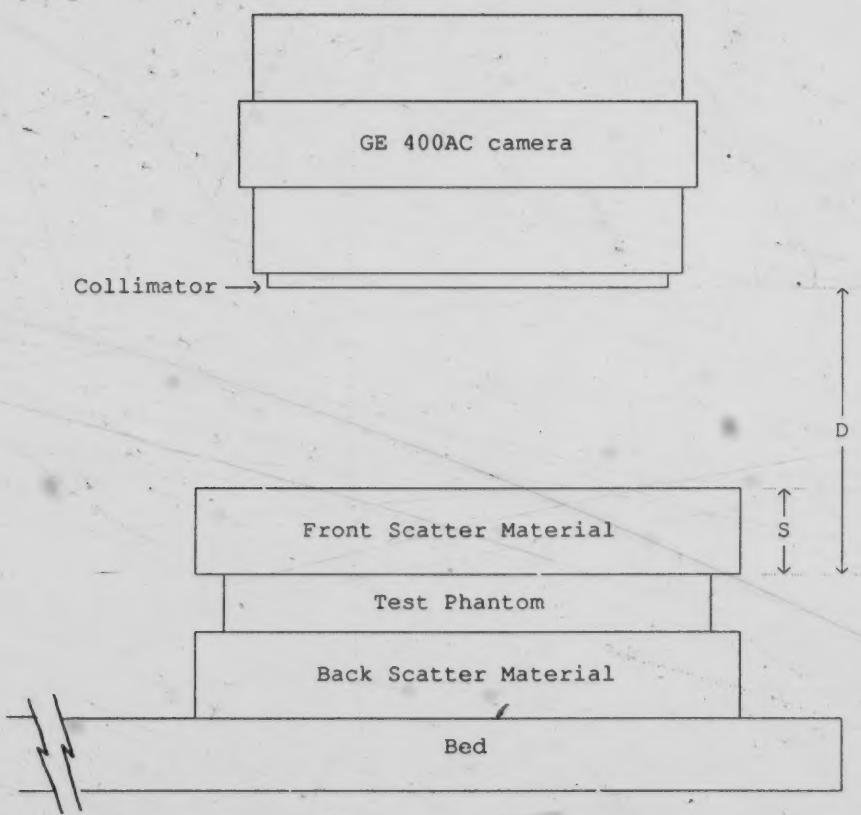

S = Scattering Material Thickness

D = Camera-to-Phantom Distance

Figure 5.2 Experimental Setup

tissue, water was used as a scattering medium. Flood tanks, containing water but no activity, were used. The attenuation coefficient of Plexiglas was very close to that of water, which is in turn, similar to that of tissue.

In order to maintain the same horizontal position in the camera's field of view for all the images, the back scatter tank was placed on the GE camera's bed and the phantom was placed on top of the scatter tank. The phantom and the scattering material were securely taped in position.

The gamma camera head is mounted on a counter balanced arm. As a result, when raising or lowering the camera, the camera also moves horizontally. In order to prevent this horizontal displacement when increasing the camera-to-phantom distance, the bed, rather the camera, was moved. As the bed was moved downward, flood tanks were inserted as front scatter material.

Without the front scatter material and with the camera in contact with the phantom (i.e. D=0cm and S=0cm) one image was acquired to 100 million counts. This was the maximum count that could be acquired because at this count level, the "hottest" pixels reached the maximum count of 65535. This high count image acquired at the camera face was the reference image to which all the other images were to be compared.

The maximum camera-to-phantom distance that could be obtained was 22cm. Distances of 0cm, 5.5cm, 10cm, and 20cm were chosen. These were typical of clinical imaging distances. One or two scatter tanks were inserted to simulate the amount of scatter seen in clinical images. Each set of data consisted of three images. The images were acquired to 10 million counts, 1 million counts, and 0.1 million

counts. This, again, bracketed the range of counts on a per pixel basis normally seen in clinical images. Table 5.1 summarizes the variation of the three imaging parameters.

Image#	Counts	Distance	Scatter
Reference	100M	0 cm	0 cm
1	10M	0 cm	0 cm
2	1M	0 cm	0 cm
3	100K	0 cm	0 cm
4	10M	5.5 cm	5.5 cm
5	1M	5.5 cm	5.5 cm
6	100K	5.5 cm	5.5 cm
7	10M	10 cm	5.5 cm
8	1M	10 cm	5.5 cm
9	100K	10 cm	5.5 cm
10	10M	20 cm	5.5 cm
11	1M	20 cm	5.5 cm
12	100K	20 cm	5.5 cm
13	10M	20 cm	11 cm
14	1M	20 cm	11 cm
15	100K	20 cm	11 cm

Table 5.1 Imaging Parameters for ^{99m}Tc study

5.3.2 Experiment II

Experiment II is similar to experiment I except that the medium energy isotope, indium-111, was used to fill the flood tank and the test phantom, and the Medium Energy Standard Parallel (MESP) collimator was installed on the camera. Some changes were made in the imaging parameters as outlined below.

5.3.2.1 Part a

The objective of the first part of the second experiment was to

characterize the noise in medium energy images. The flood images were acquired to total counts of 10 thousand, 100 thousand, 500 thousand, 2.5 million, 12.5 million and 75 million counts. The images were acquired in the same way as in experiment Ia.

5.3.2.2 Part b

The objective of the second part of the second experiment was to observe the effect of varying the total count, varying the camera to object distance, varying the amount of scattering material, and the application of filters on images acquired with indium-111.

Clinically, studies involving indium generally have lower counts than technetium studies because lower quantities of activity are administered to patients. In these experiments, therefore, the total image counts were reduced compared to experiment Ib. The images were acquired to 100 thousand, 500 thousand and 2.5 million counts. The reference image was acquired to 100 million counts.

The imaging distances were changed slightly to increase the number of images with scatter. The 10cm distance was increased to 11cm so that an image with two scatter tanks could be acquired.

Table 5.2 summarizes the imaging parameters.

5.4 Procedure for Filtering Test Phantom Images

A program to filter the images was written in VAX Fortran. The program read the Gamma-11 image file, filtered the images with either the Butterworth filter or the image dependent Metz filter, and stored

Image #	Counts	Distance	Scatter
Reference	100M	0cm	0cm
1	2.5M	0cm	0cm
2	500K	0cm	0cm
3	100K	0cm	0cm
4	2.5M	5.5cm	5.5cm
5	500K	5.5cm	5.5cm
6	100K	5.5cm	5.5cm
7	2.5M	5.5cm	0cm
8	500K	5.5cm	0cm
9	100K	5.5cm	0cm
10	2.5M	11cm	0cm
11	500K	11cm	0cm
12	100K	11cm	0cm
13	2.5M	11cm	5.5cm
14	500K	11cm	5.5cm
15	100K	11cm	5.5cm
16	2.5M	11cm	11cm
17	500K	11cm	11cm
18	100K	11cm	11cm
19	2.5M	20cm	11cm
20	500K	20cm	11cm
21	100K	20cm	11cm
22	2.5M	20cm	5.5cm
23	500K	20cm	5.5cm
24	100K	20cm	5.5cm
25	2.5M	20cm	0cm
26	500K	20cm	0cm
27	100K	20cm	0cm

Table 5.2 Imaging parameters for ^{111}In study

the filtered image. The raw and the filtered images were then analyzed.

5.5 Procedure for Analysis of Images

The images from both experiment I and experiment II were analyzed in the same manner. Three methods of analysis were used. The first

was a quantification of noise; the second was a contrast measurement; and the third was a measure of the general "quality" of an image.

5.5.1 Noise

The first feature of the images to be studied was noise. The noise in raw and filtered flood images was characterized by the standard deviation of the pixel counts. To avoid edge effects created by the filters, only a 32 by 32 pixel region in the centre of the flood images was used in the standard deviation calculations.

The flood images were filtered using a Butterworth and several different Metz filters. The Metz filter procedure discussed in chapter IV was not used because of the way it automatically picked the cutoff frequency from the power spectrum of the image. The Metz filtering program was modified to override the automatic X parameter calculation and the Metz filter was implemented for various clinically significant cutoff frequencies. Since the F_C/F_N parameter in the technetium test phantom studies varied from 0.24 to 0.54, where F_C is the cutoff frequency and F_N is the Nyquist frequency, values that bracketed this range were chosen. For the indium test phantom images, F_C/F_N varied from 0.23 to 0.50.

5.5.2 Contrast

It was also desired to see how the contrast of the test phantom images was affected by the different imaging parameters and filters. The contrasts of the various sized hot and cold spots in all the images were calculated according to equations 5.1 and 5.2.

$$\text{Cold Spot Contrast} = \frac{(\text{Cold count} - \text{Surrounding count})}{\text{Surrounding count}} \cdot 100\% \quad (5.1)$$

$$\text{Hot Spot Contrast} = \frac{(\text{Hot count} - \text{Surrounding count})}{\text{Surrounding count}} \cdot 100\% \quad (5.2)$$

Hot spots gave positive contrast values while cold spots gave negative contrast values. Since pixel values were always positive, the contrast of the cold spots was always between -100% and 0%.

The pixel used for the contrast calculation was chosen by picking the maximum or the minimum pixel in the central region of each hot or cold spot respectively. The central region of each contrast spot was defined by a region of interest (ROI) drawn manually using the Gamma-11 image analysis program. The ROI's were entered on the PCS-512 work station and the regions saved in a Gamma-11 "save area" file. The save area was transferred to the VAX computer, and a program used to find the hottest and the coldest pixel in the previously defined ROIs. The central regions of the contrast spots consisted of between 4 and 12 pixels. Two large ROI's, consisting of over 200 pixels each, were used to calculate average background values around the contrast spots.

5.5.3 Comparison to Reference Image

It was desired to compare images acquired under non-ideal conditions with a high quality reference image. A high count image acquired close to the collimator face would have good spatial resolution and low noise and was therefore chosen as a reasonable approximation of a perfect image. All other images were compared to this reference image. A visual comparison of the images was used

initially. This method was considered to be too subjective, however, although clinical images in nuclear medicine are visually evaluated by a physician. A more quantitative and objective method was therefore developed to compare the images.

In order to compare an image, S(I,J), to a reference image, R(I,J), a figure of merit, Ψ, was defined such that

$$\Psi = \sum_{I,J} \frac{\left(R(I,J) - f \cdot S(I,J) \right)^2}{R(I,J)} \qquad (5.3)$$

where f is a scaling factor. This figure of merit is similar to the standard Chi-squared test statistic defined by equation 5.4.

$$\chi^2 = \sum_{I,J} \frac{\left(S(I,J) - c\, R(I,J) \right)^2}{c\, R(I,J)} \qquad (5.4)$$

where c is, again, a scaling factor.

It can be shown that $\Psi = f\chi^2$ if $c=\frac{1}{f}$. The Chi-squared test is generally used to decide if a measured set of data is consistent with an expected distribution of data. The Chi-squared statistic is independent of the amount of noise in the measured data. Thus if images with different total counts but acquired under the same imaging conditions are compared to the reference image using the Chi-squared test, the test statistic will be independent of count.

It was desired that the comparison test yield values that would indicate relative image quality, including the effects of noise. Only in this way would it be possible to compare, for example, the effect

of a particular filter to the effect of increasing the counts in an image. Therefore the figure of merit defined in equation 5.3 was used.

In equation 5.3, the comparison image is scaled up to the reference image. This scaling factor, f, can be interpreted physically as the intensity or brightness of the displayed image. It can easily be shown that the figure of merit, Ψ, is minimized when f is defined by equation 5.5.

$$f = \frac{\sum_{I,J} S(I,J)}{\sum_{I,J} \frac{S^2(I,J)}{R(I,J)}} \qquad (5.5)$$

In practice, the summations in equations 5.3 and 5.5 were calculated using only those pixels in the reference image which had a count higher than 5% of the highest pixel in the image. This restricted the summations to pixels inside the phantom.

In order to compare the effectiveness of different filters, a quantity representing the improvement in the comparison factor between an unfiltered (raw) and filtered image was defined. This "improvement index" was calculated according to equation 5.6.

$$\text{Improvement Index} = \frac{\Psi_{raw} - \Psi_{filtered}}{\Psi_{raw}} \cdot 100\% \qquad (5.6)$$

5.6 Results

5.6.1 Noise

Figure 5.3 gives the standard deviation in percent of the pixel values for the raw, Butterworth and various Metz filtered technetium noise images. Figure 5.4 shows the percent standard deviation of the raw and filtered indium noise images.

5.6.2 Contrast

Figures 5.5 and 5.6 show the reference, raw and filtered images of the technetium and indium filled test phantom. Figure 5.7 shows the contrast of the technetium reference image. Figures 5.8 through 5.10 show the variation in the contrast as a function of counts, distance and scatter. Figures 5.11 to 5.14 show the effect of filtering on image contrast.

Figure 5.15 shows the contrast of the indium reference image. Figures 5.16 to 5.18 show the effects of variations in the imaging parameters. Figures 5.19 to 5.22 show the effect of filtering on the indium images.

5.6.3 Comparison Test

Figure 5.23 shows the comparison factor for the raw technetium images. Figure 5.24 shows the effect of filtering on the technetium images' comparison factors. Figure 5.25 shows the improvement index of the filtered technetium images for various counts.

Figure 5.26 shows the comparison factors for the raw indium images and figure 5.27 shows the effect of filtering the images.

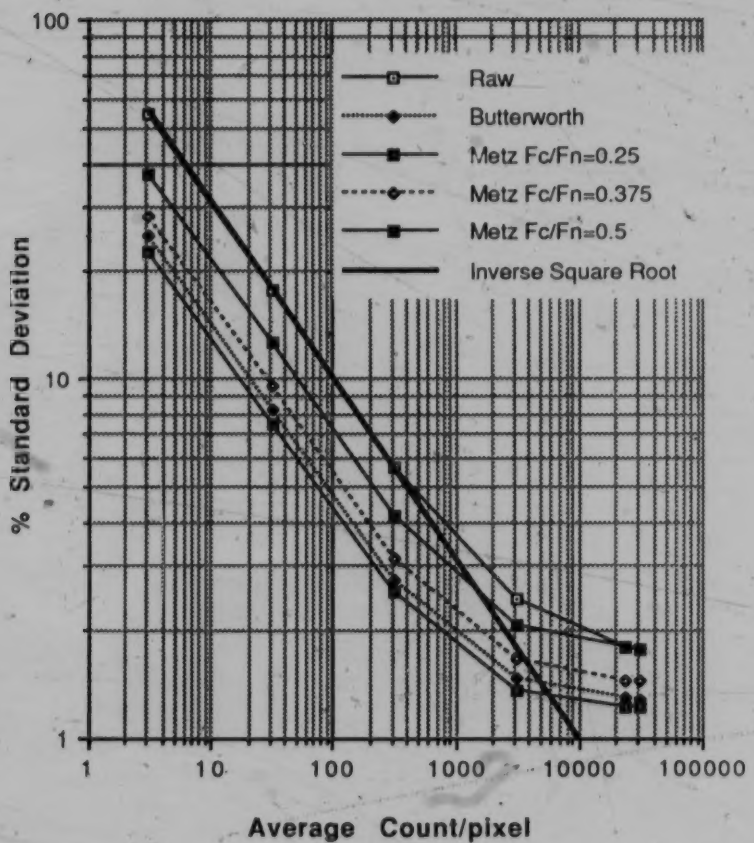

Figure 5.3 Standard deviation of pixel counts for raw and filtered, technetium flood tank images.

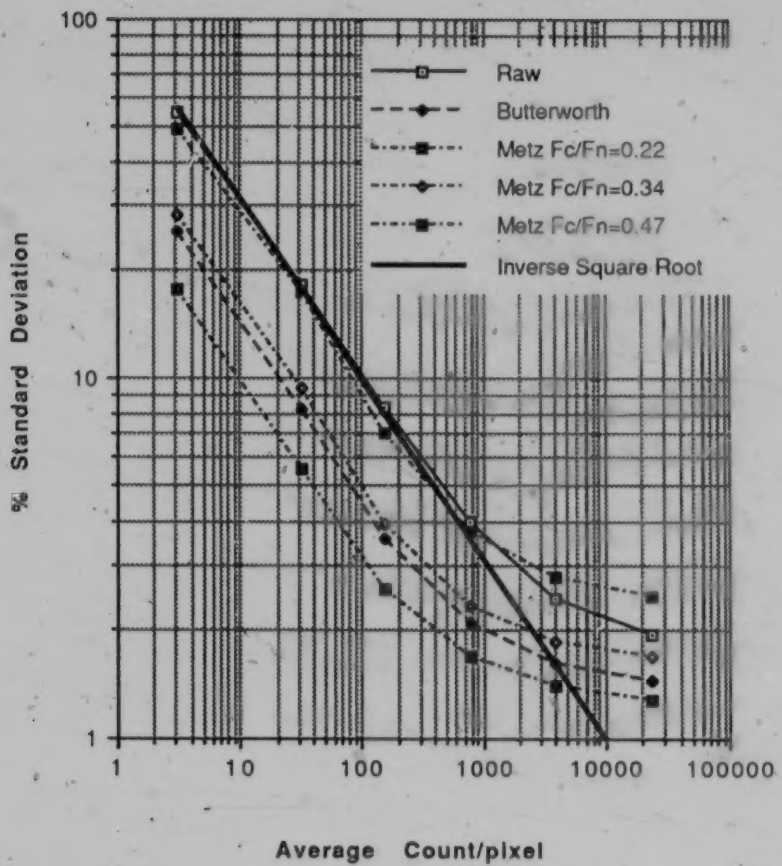

Figure 5.4 Standard deviation of pixel counts for raw and filtered, indium flood tank images.

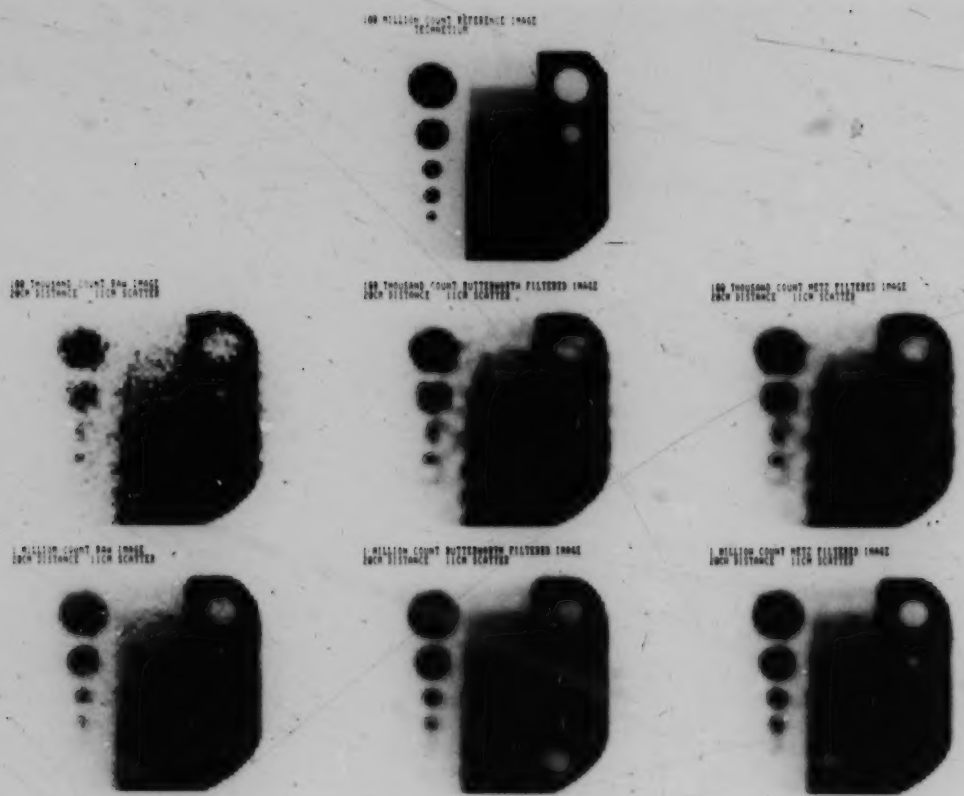

Figure 5.5 Photograph of Technetium filled test phantom reference image with raw, Butterworth filtered, and Metz filtered images acquired to 100 thousand and 1 million counts.

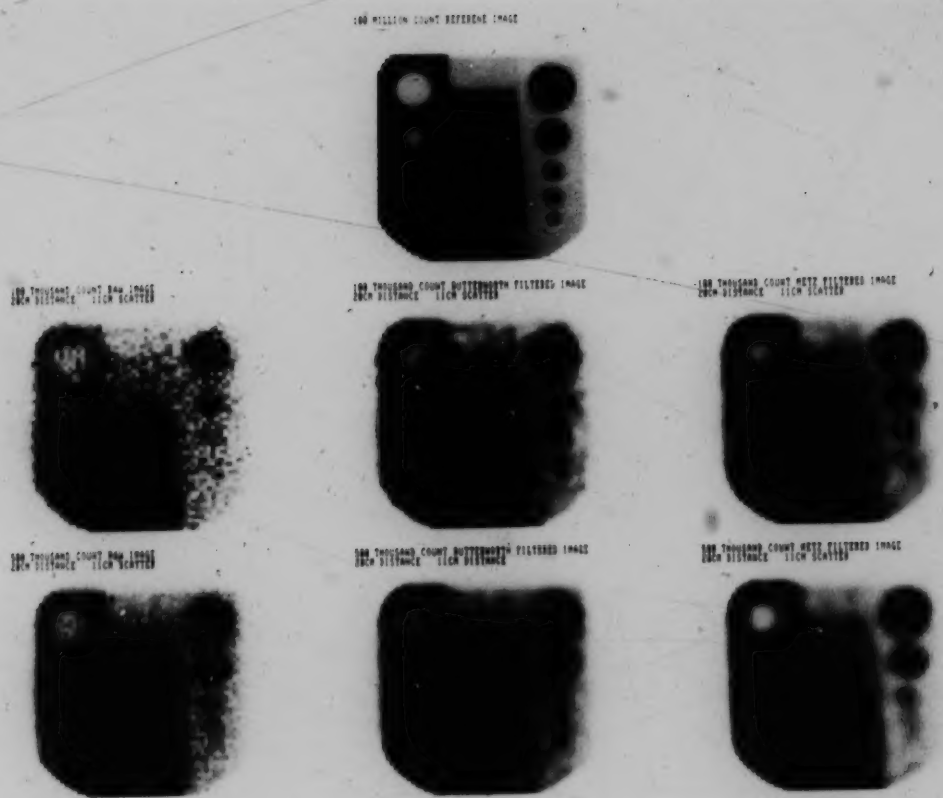

Figure 5.6 Photograph of Indium filled test phantom reference image with raw, Butterworth filtered, and Metz filtered images acquired to 100 thousand and 500 thousand counts.

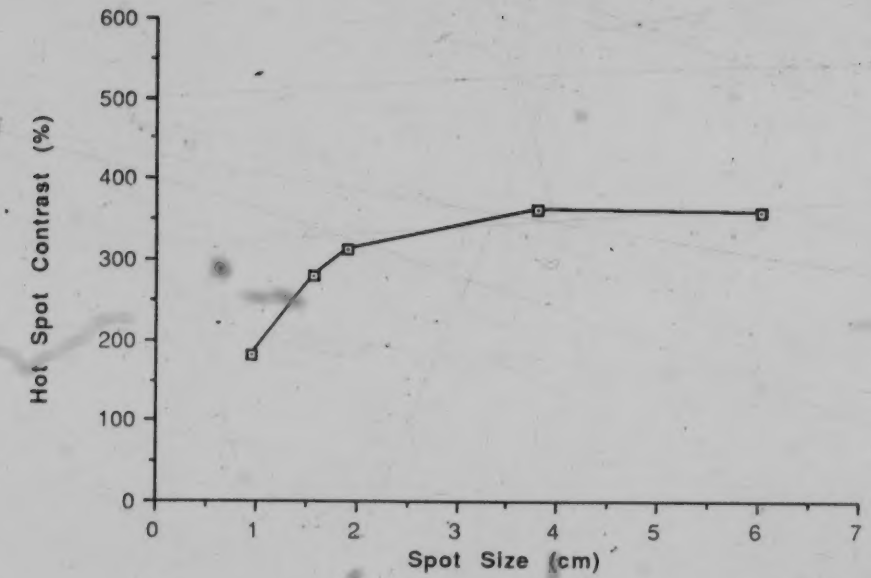

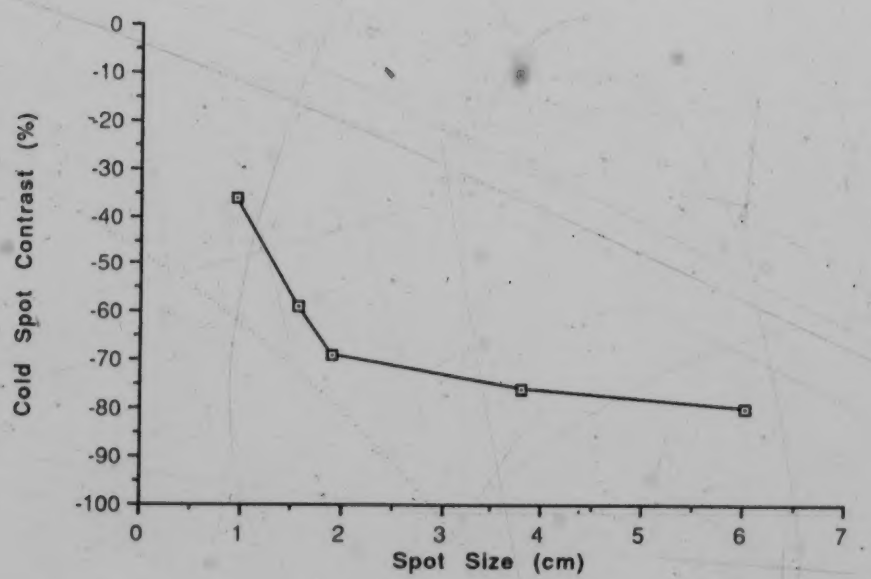

Figure 5.7 Hot and cold spot contrast for technetium filled test phantom reference image.

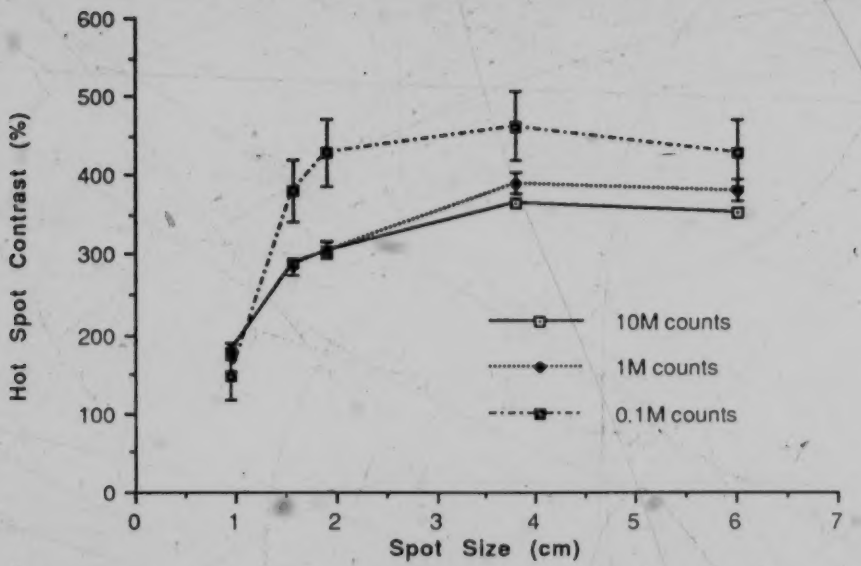

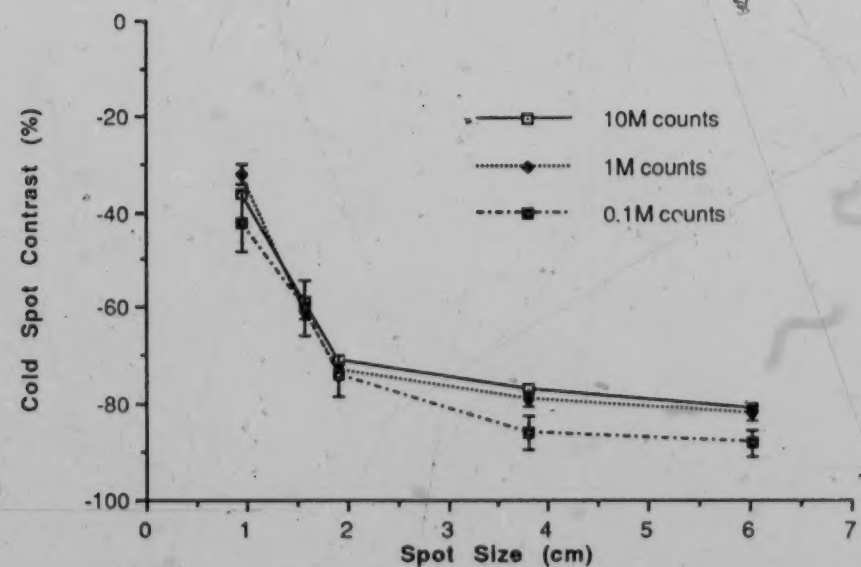

Figure 5.8 Hot and cold spot contrast of technetium filled test phantom images acquired at camera face plotted for various counts.

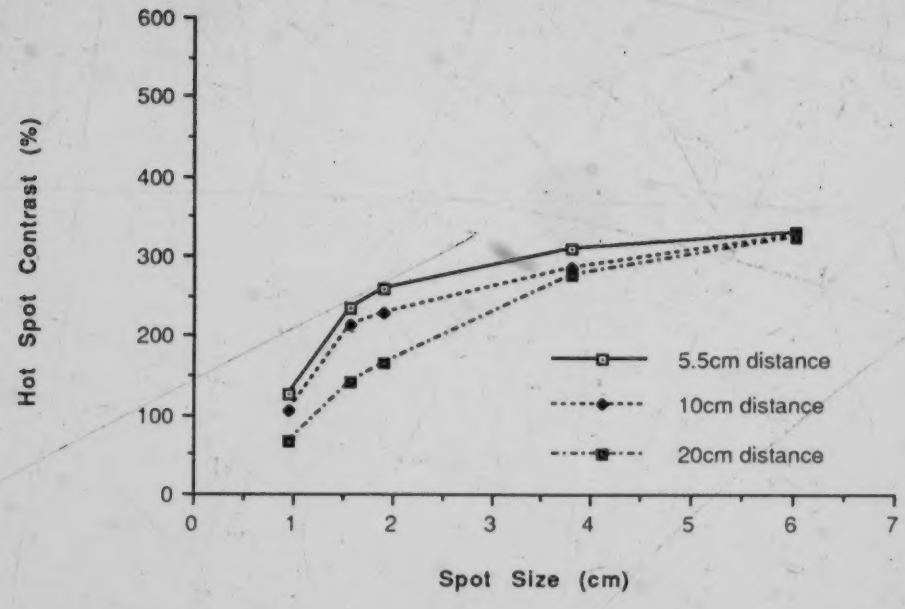

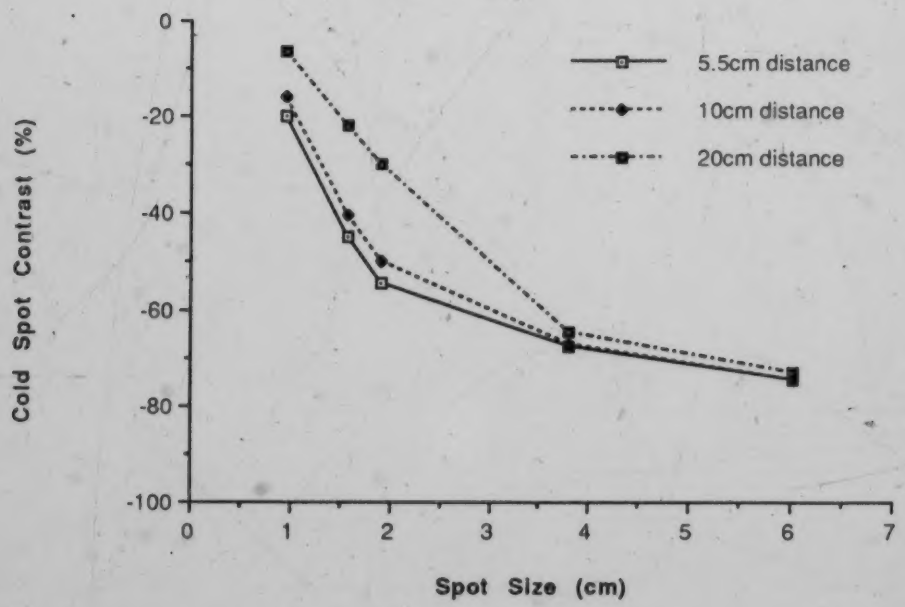

Figure 5.9 Hot and cold spot contrast for 10 million count, technetium filled test phantom images acquired with 5.5cm scatter material plotted for various distances.

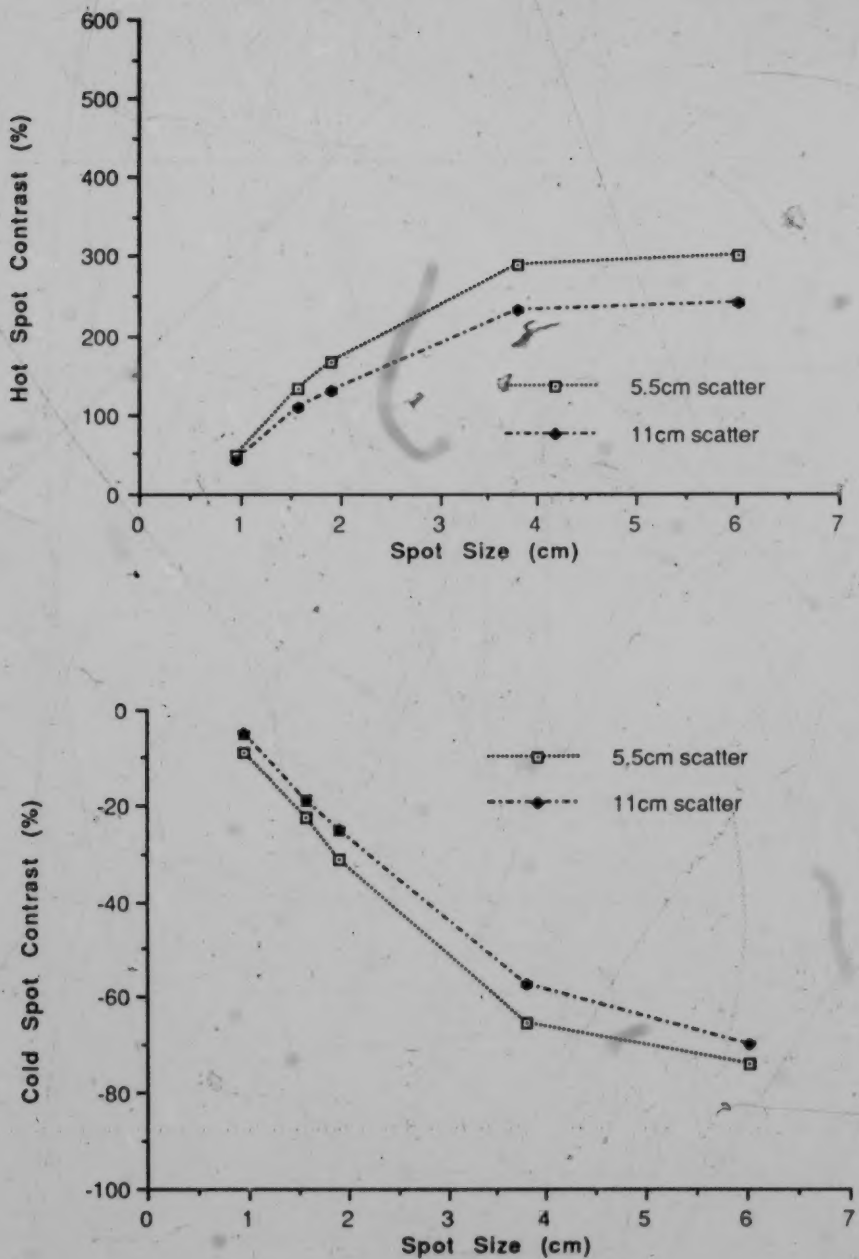

Figure 5.10 Hot and cold spot contrast for 10 million count, technetium filled test phantom images acquired at 20cm plotted for various amounts of scatter material.

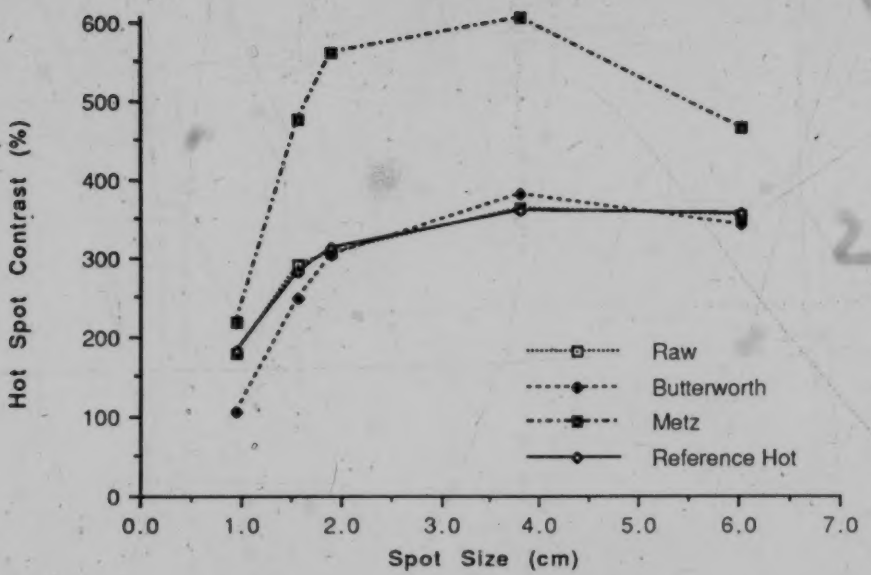

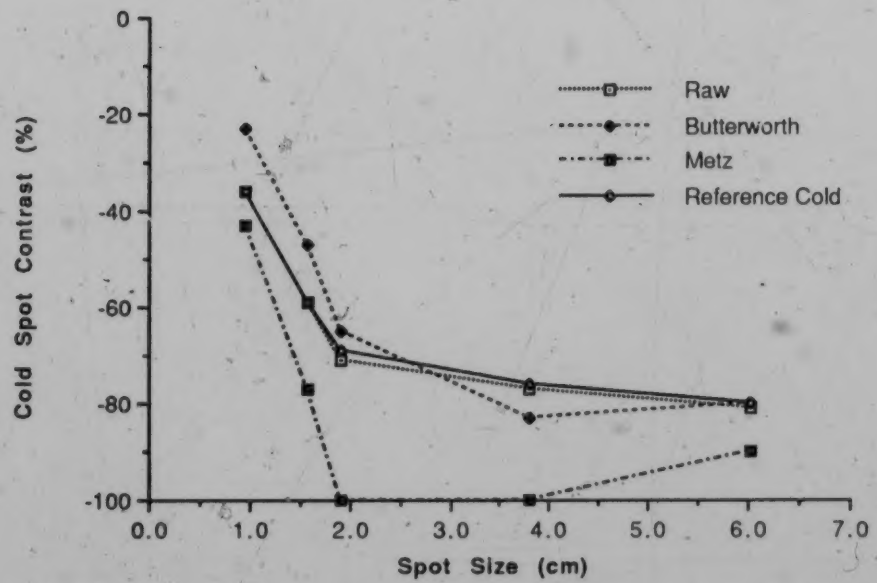

Figure 5.11 Hot and cold spot contrast for 10 million count, technetium filled test phantom images acquired at camera face filtered with Butterworth and Metz filters.

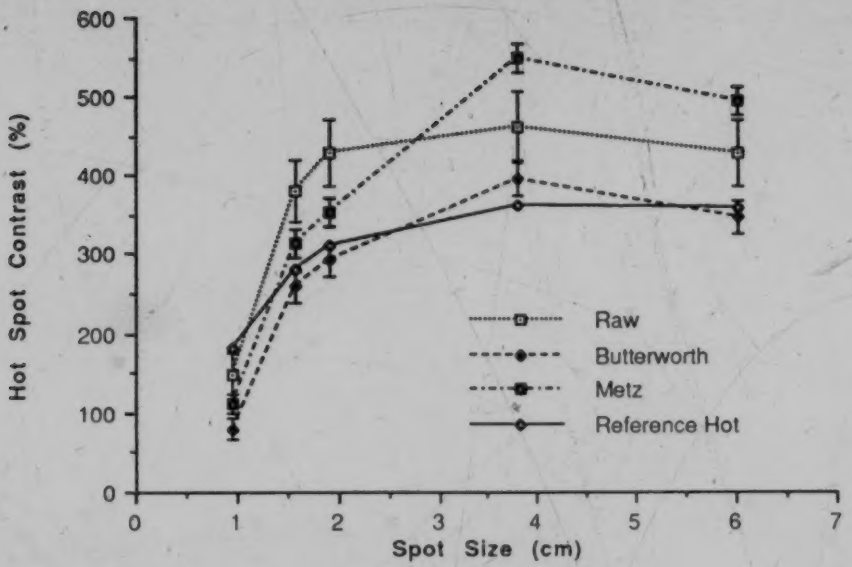

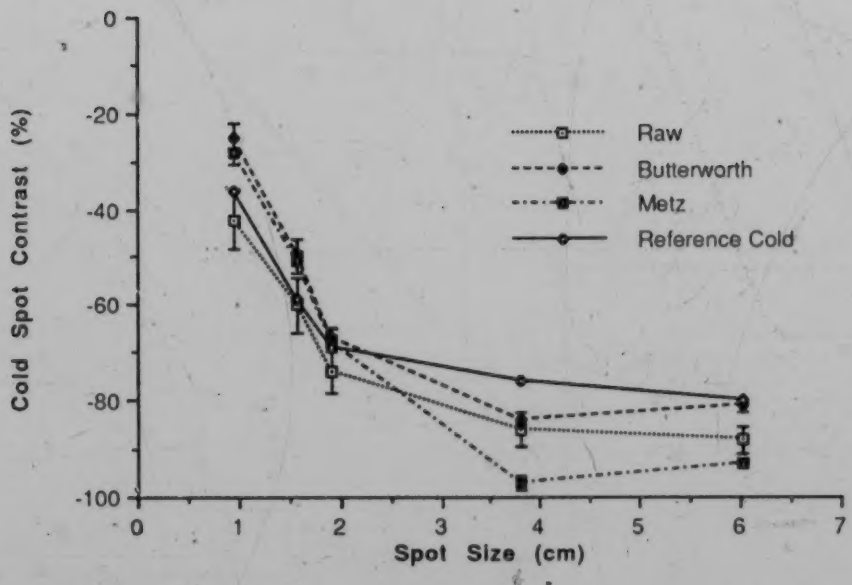

Figure 5.12 Hot and cold spot contrast for 100 thousand count, technetium filled test phantom images acquired at camera face filtered with Butterworth and Metz filters.

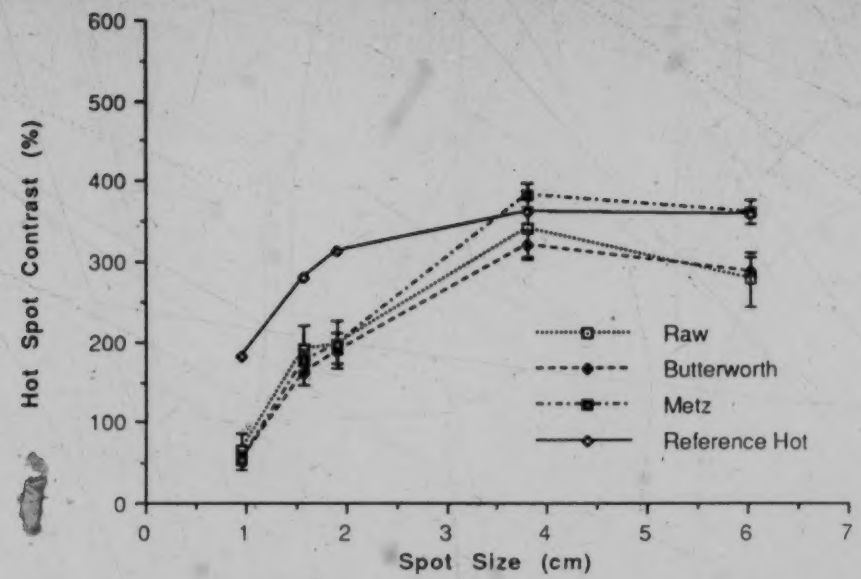

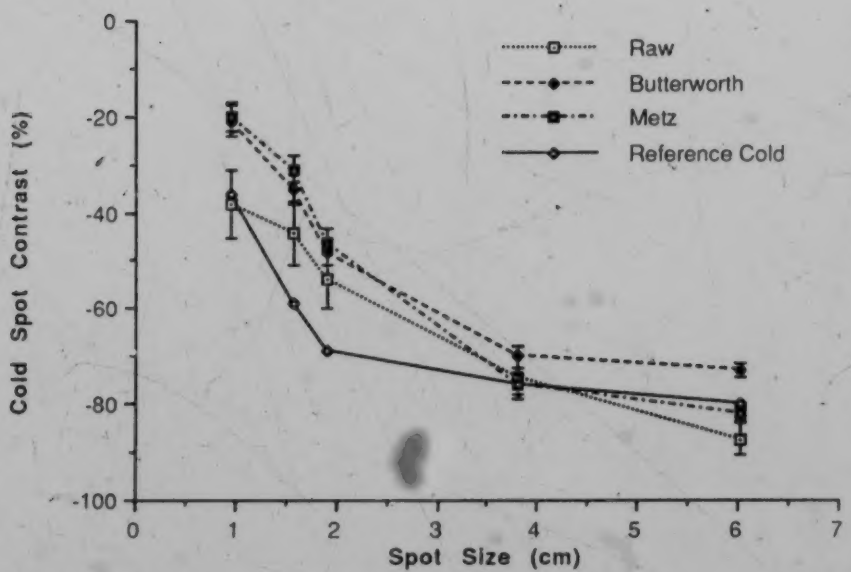

Figure 5.13 Hot and cold spot contrast for 100 thousand count, technetium filled test phantom images acquired at 10cm with 5.5cm scatter material filtered with Butterworth and Metz filters.

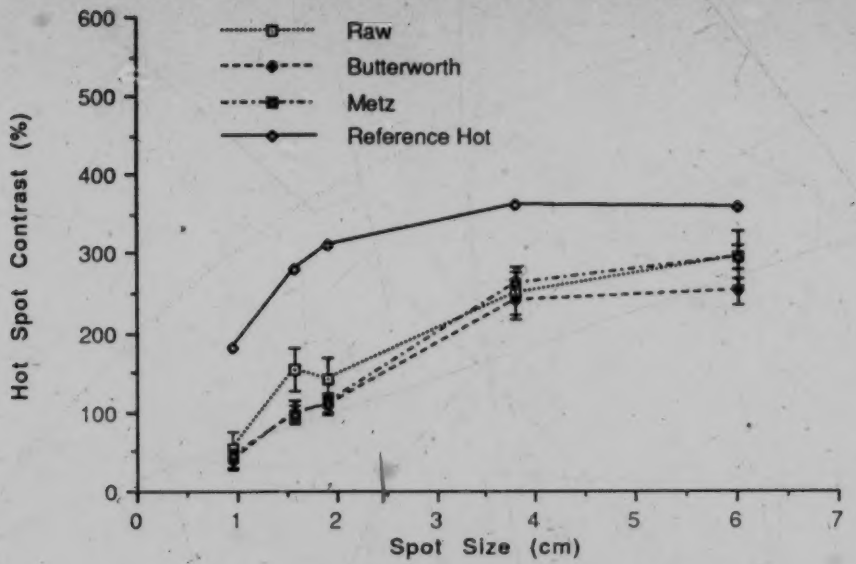

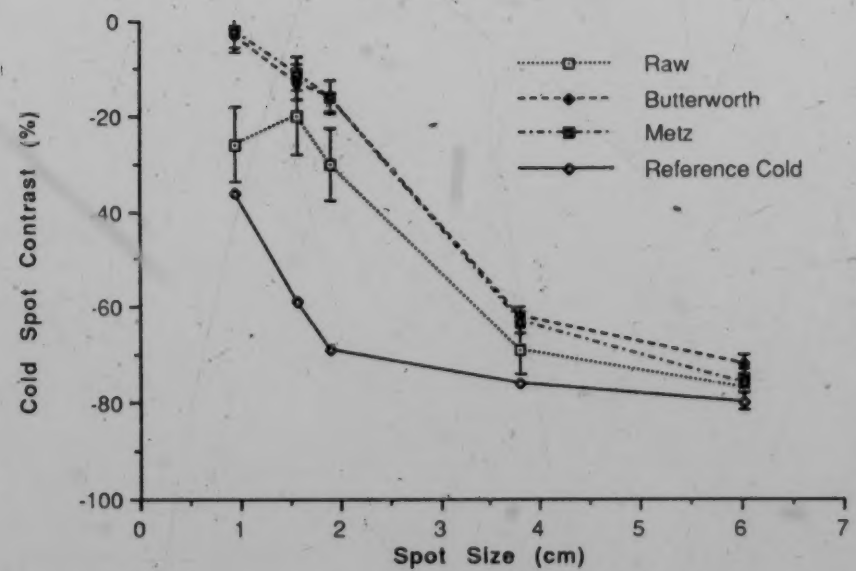

Figure 5.14 Hot and cold spot contrast for 100 thousand count, technetium filled test phantom images acquired at 20cm with 11cm scatter material filtered with Butterworth and Metz filters.

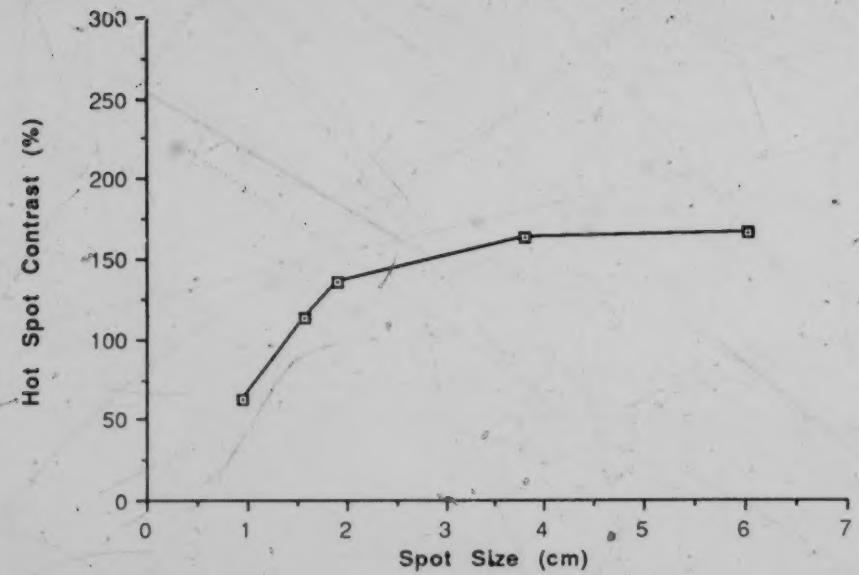

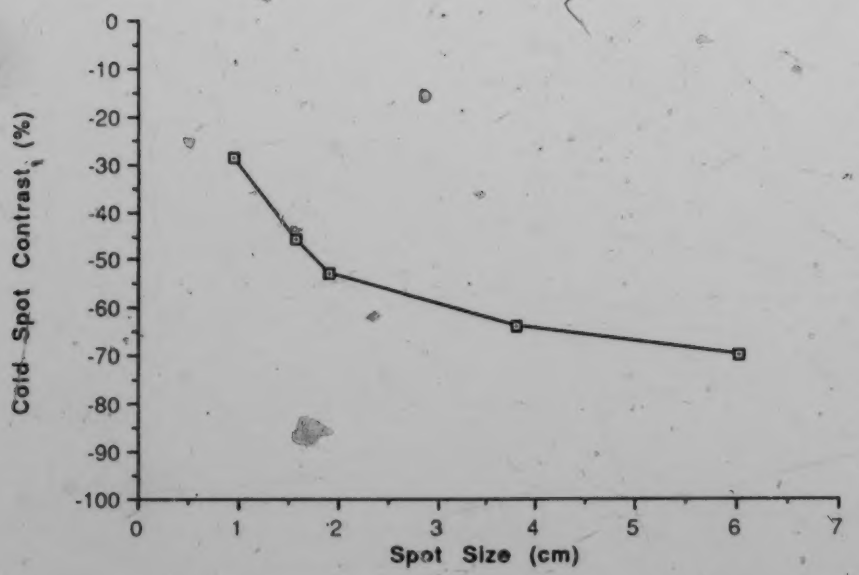

Figure 5.15 Hot and cold spot contrast for indium filled test phantom reference image.

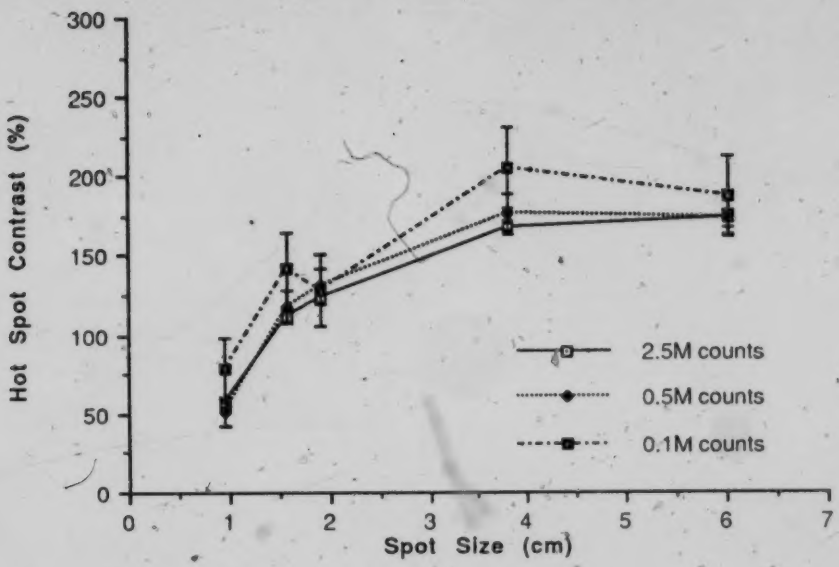

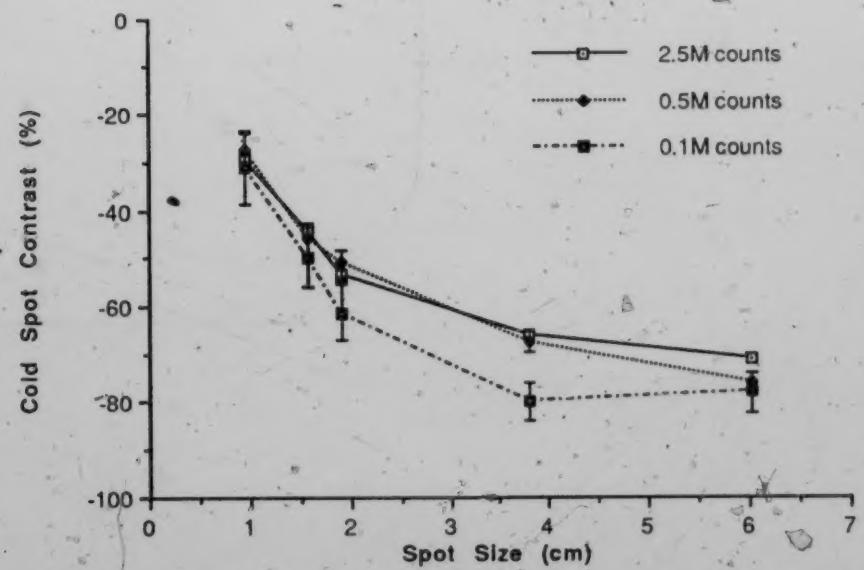

Figure 5.16 Hot and cold spot contrast of indium filled test phantom images acquired at camera face plotted for various counts.

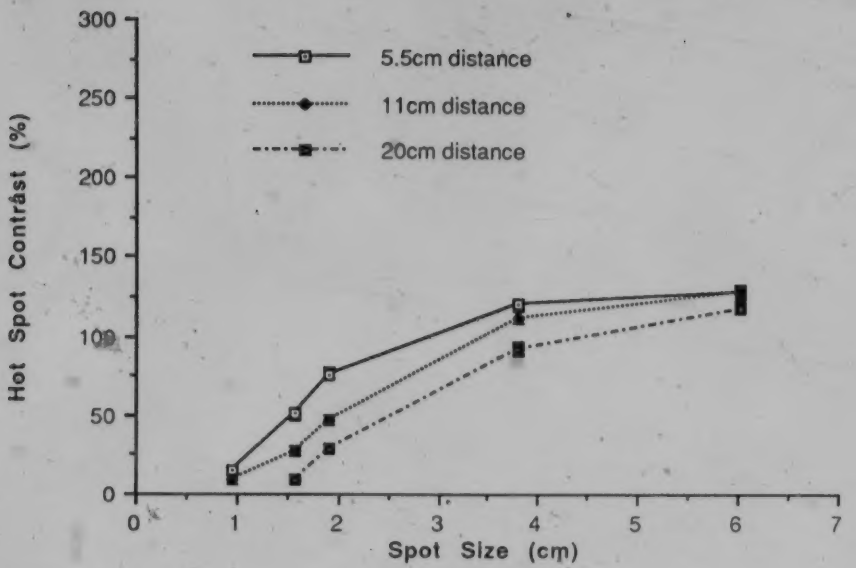

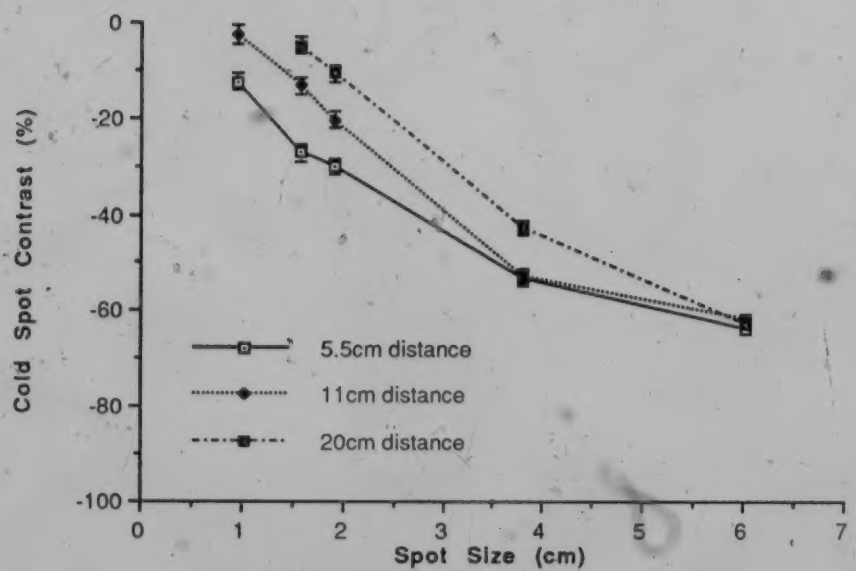

Figure 5.17 Hot and cold spot contrast for 10 million count, indium filled test phantom images acquired with 5.5cm scatter material plotted for various distances.

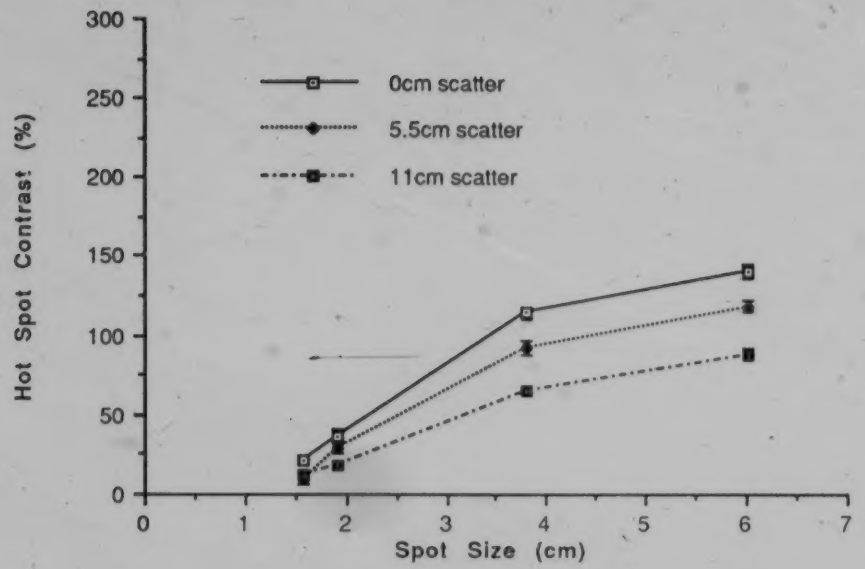

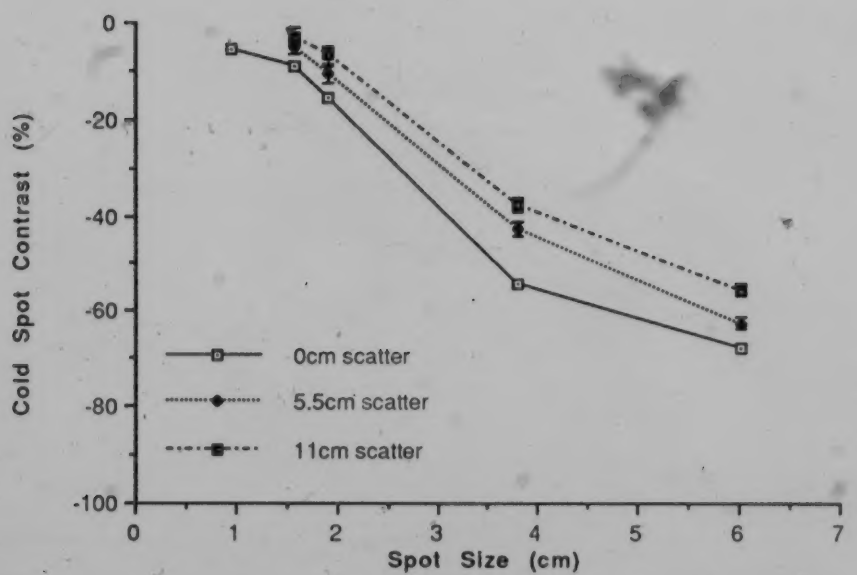

Figure 5.18 Hot and cold spot contrast for 10 million count, indium filled test phantom images acquired at 20cm plotted for various amounts of scatter material.

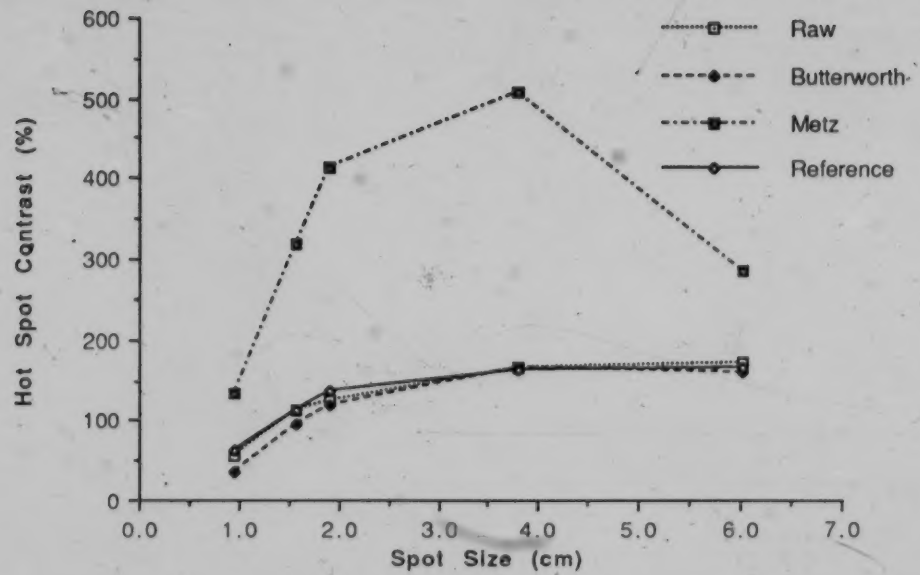

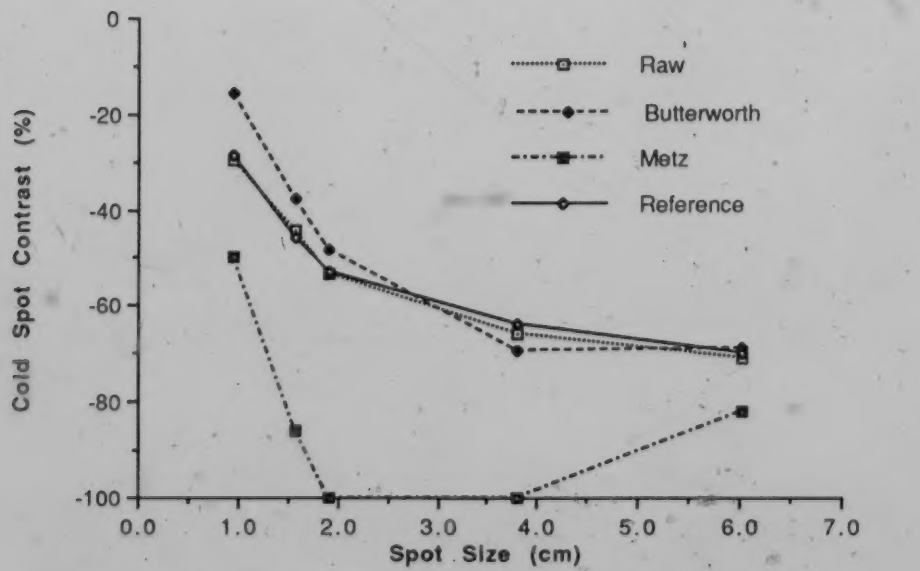

Figure 5.19 Hot and cold spot contrast for 10 million count, indium filled test phantom images acquired at camera face filtered with Butterworth and Metz filters.

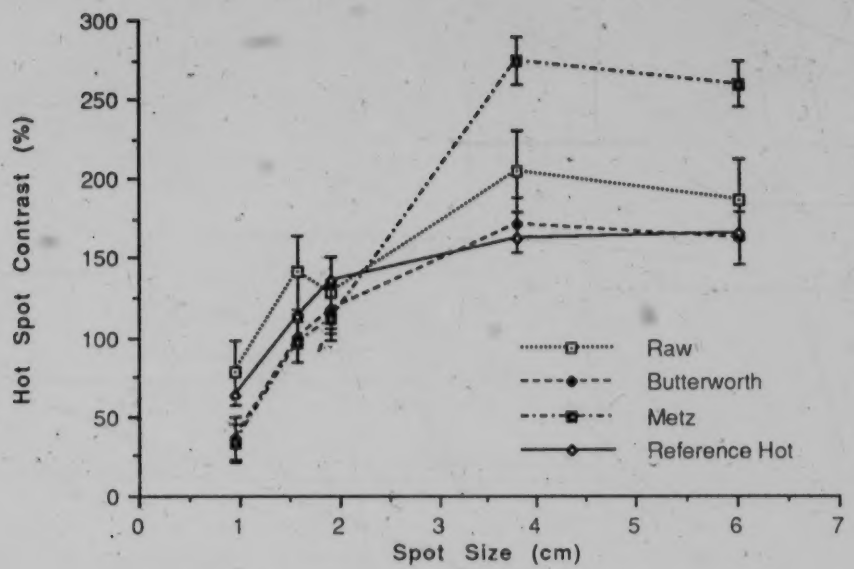

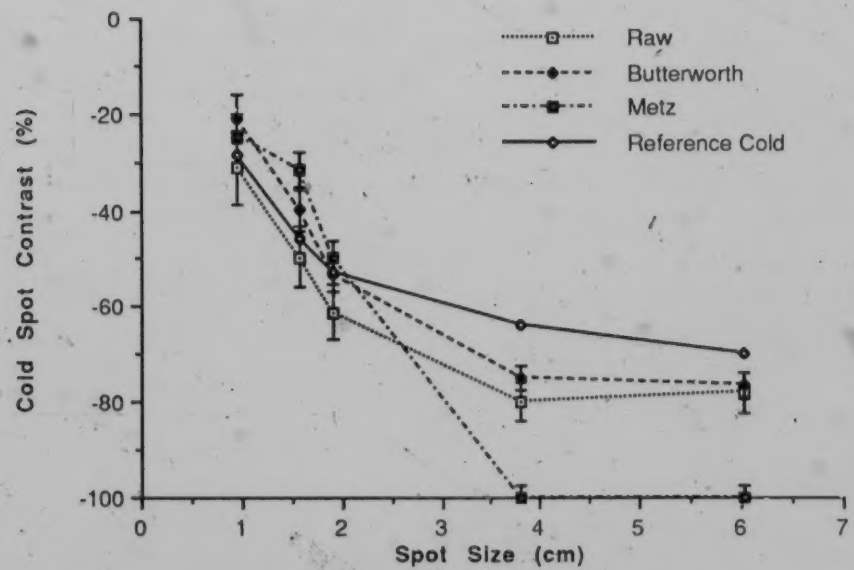

Figure 5.20 Hot and cold spot contrast for 100 thousand count, indium filled test phantom images acquired at camera face filtered with Butterworth and Metz filters.

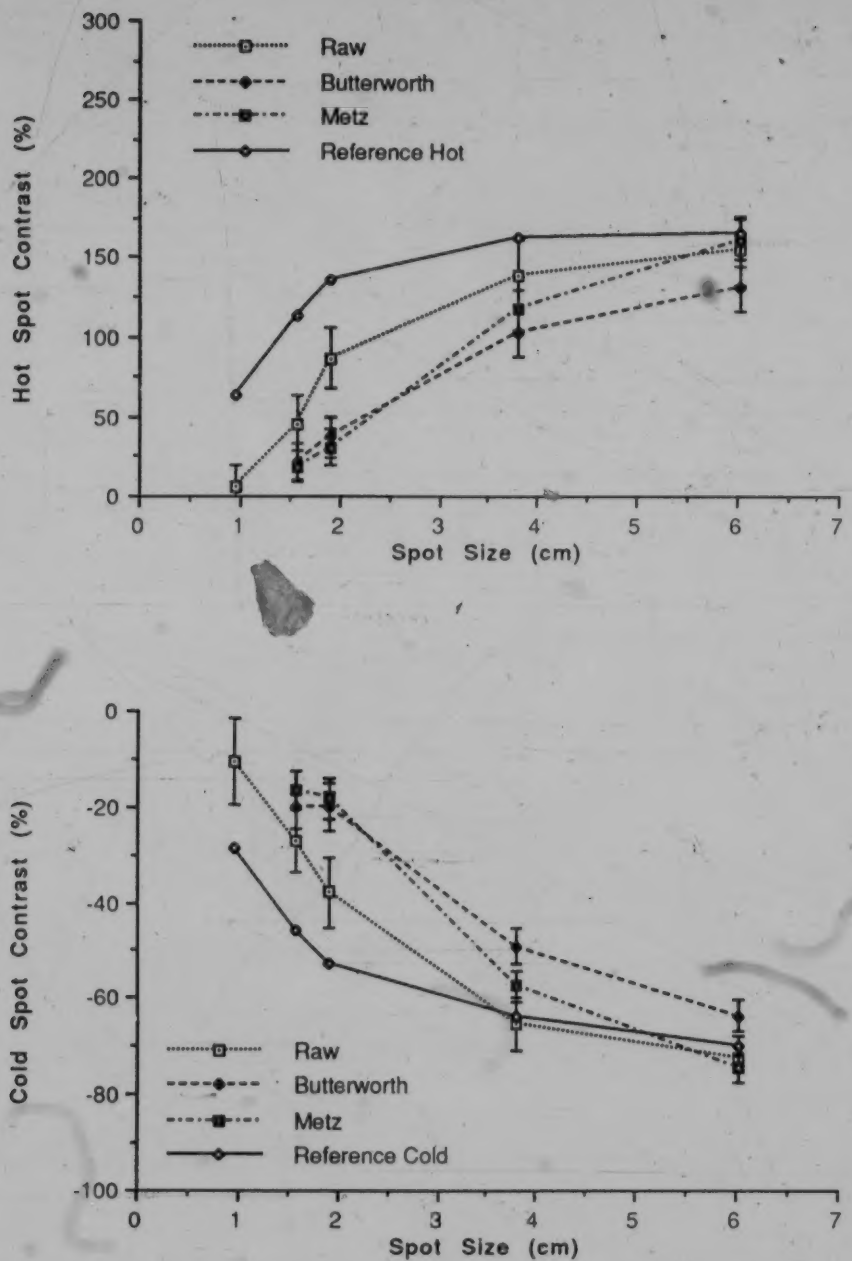

Figure 5.21 Hot and cold spot contrast for 100 thousand count, indium filled test phantom images acquired at 11cm with 5.5cm scatter material filtered with Butterworth and Metz filters.

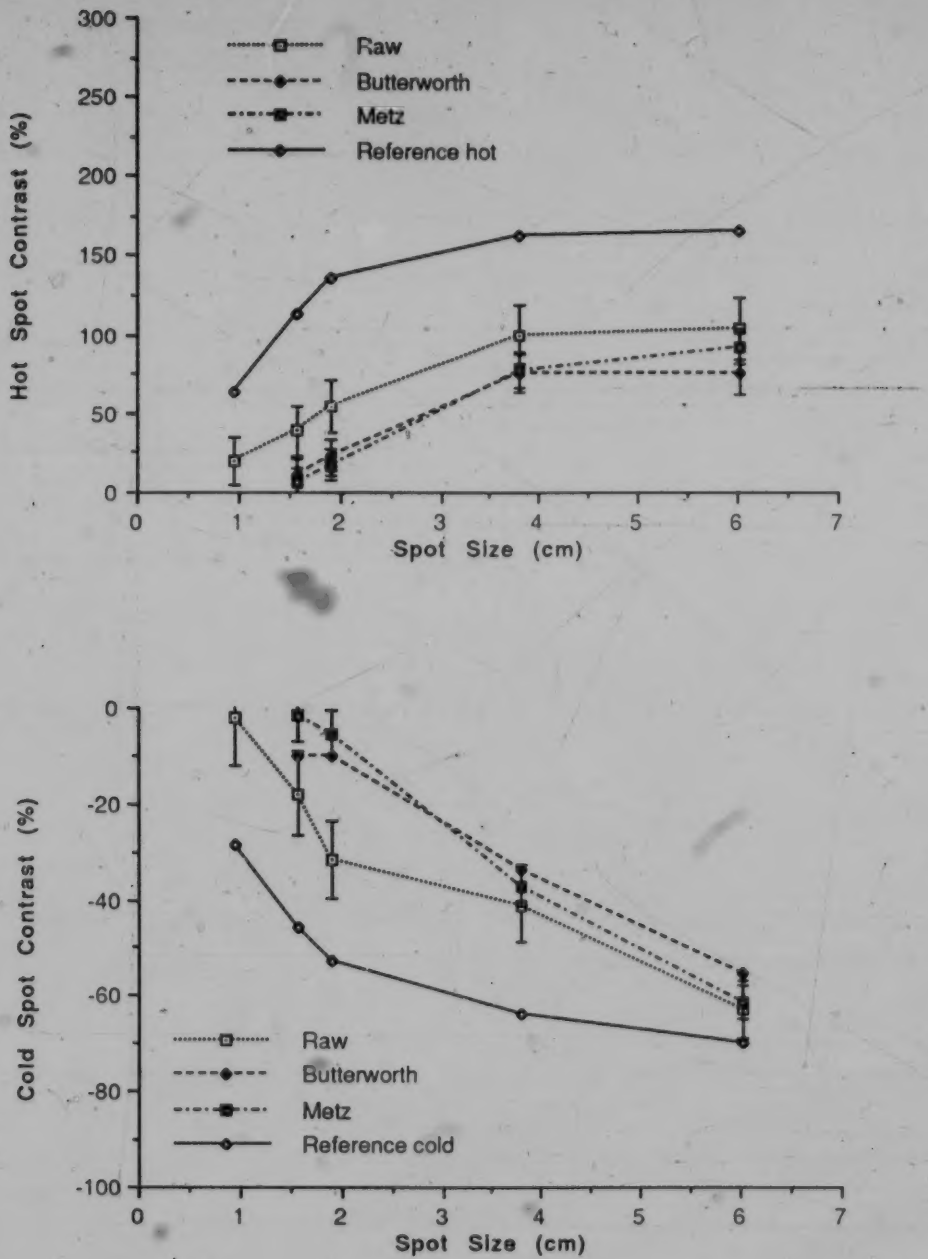

Figure 5.22 Hot and cold spot contrast for 100 thousand count, indium filled test phantom images acquired at 20cm with 11cm scatter material filtered with Butterworth and Metz filters.

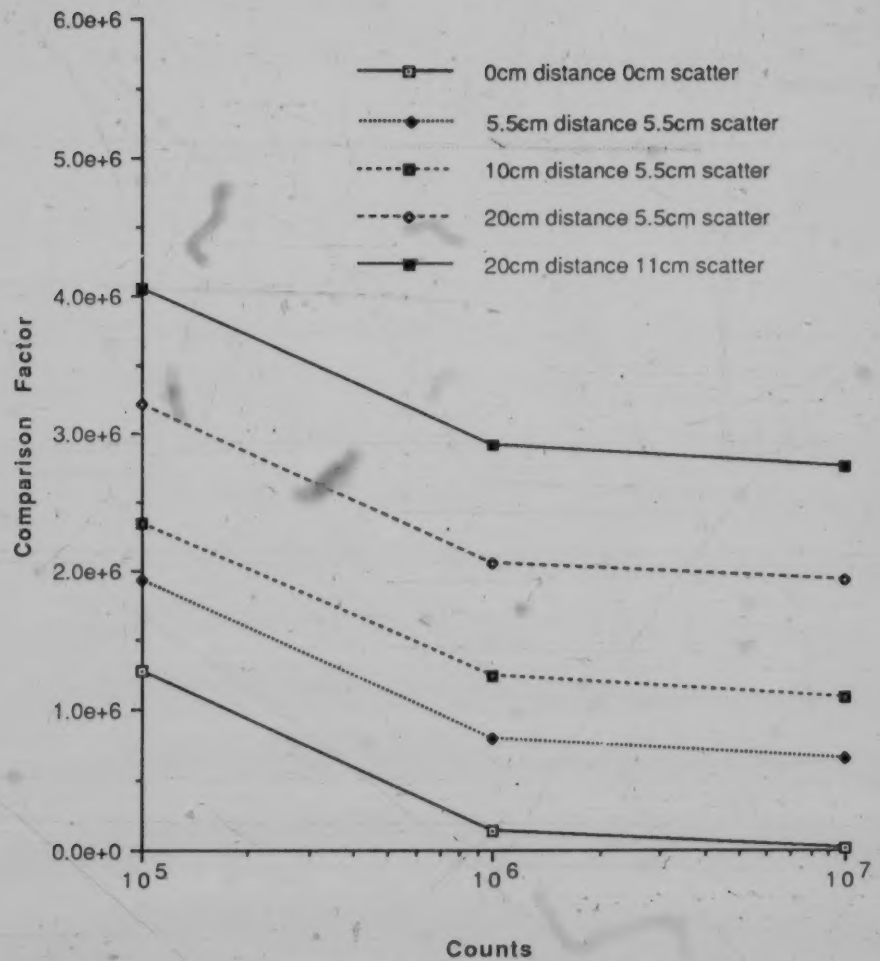

Figure 5.23 Comparison factor for raw technetium filled test phantom images acquired under various conditions plotted as a function of counts.

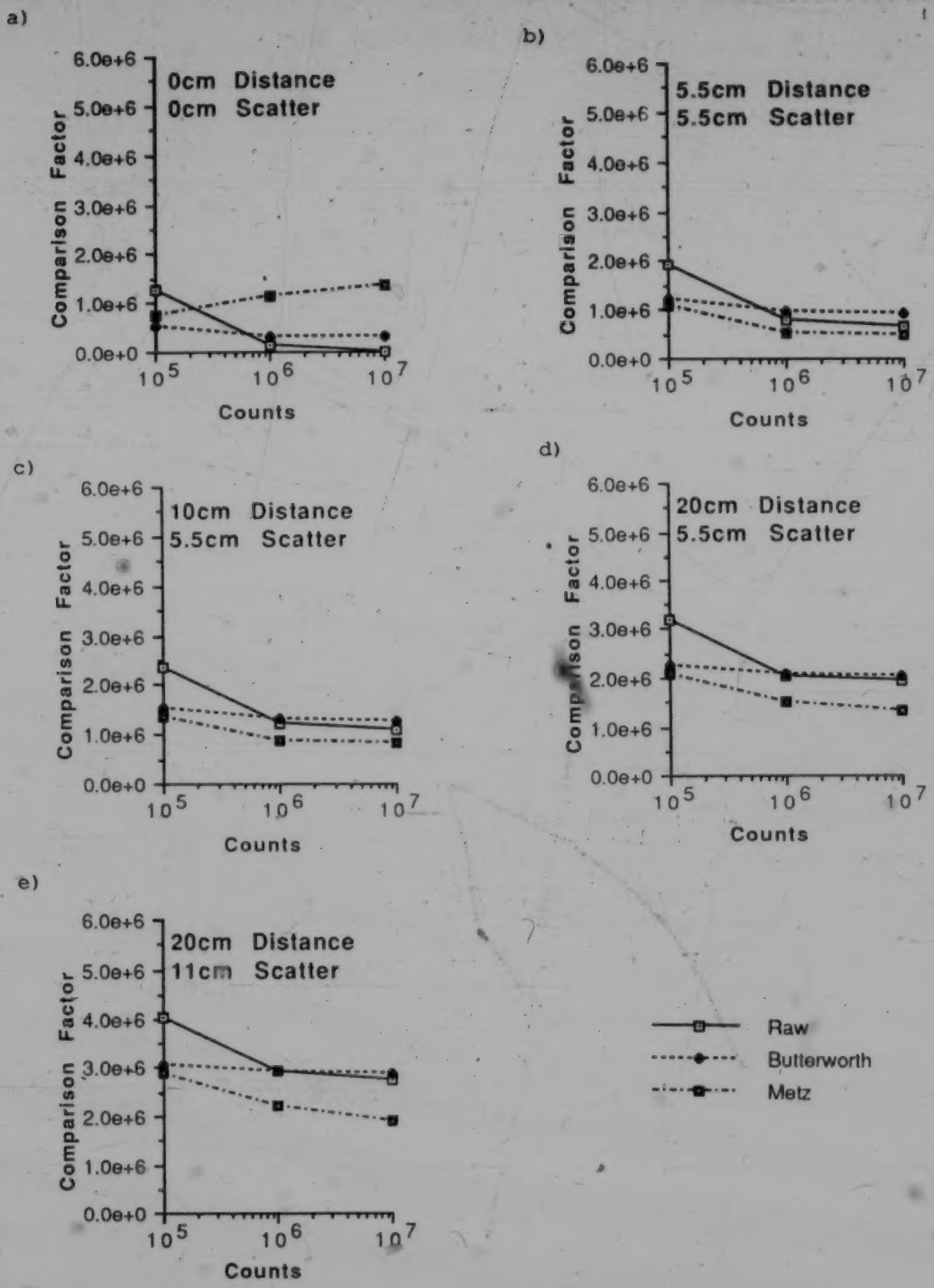

Figure 5.24 Effect of Butterworth and Metz filters on comparison factor of technetium filled test phantom images.

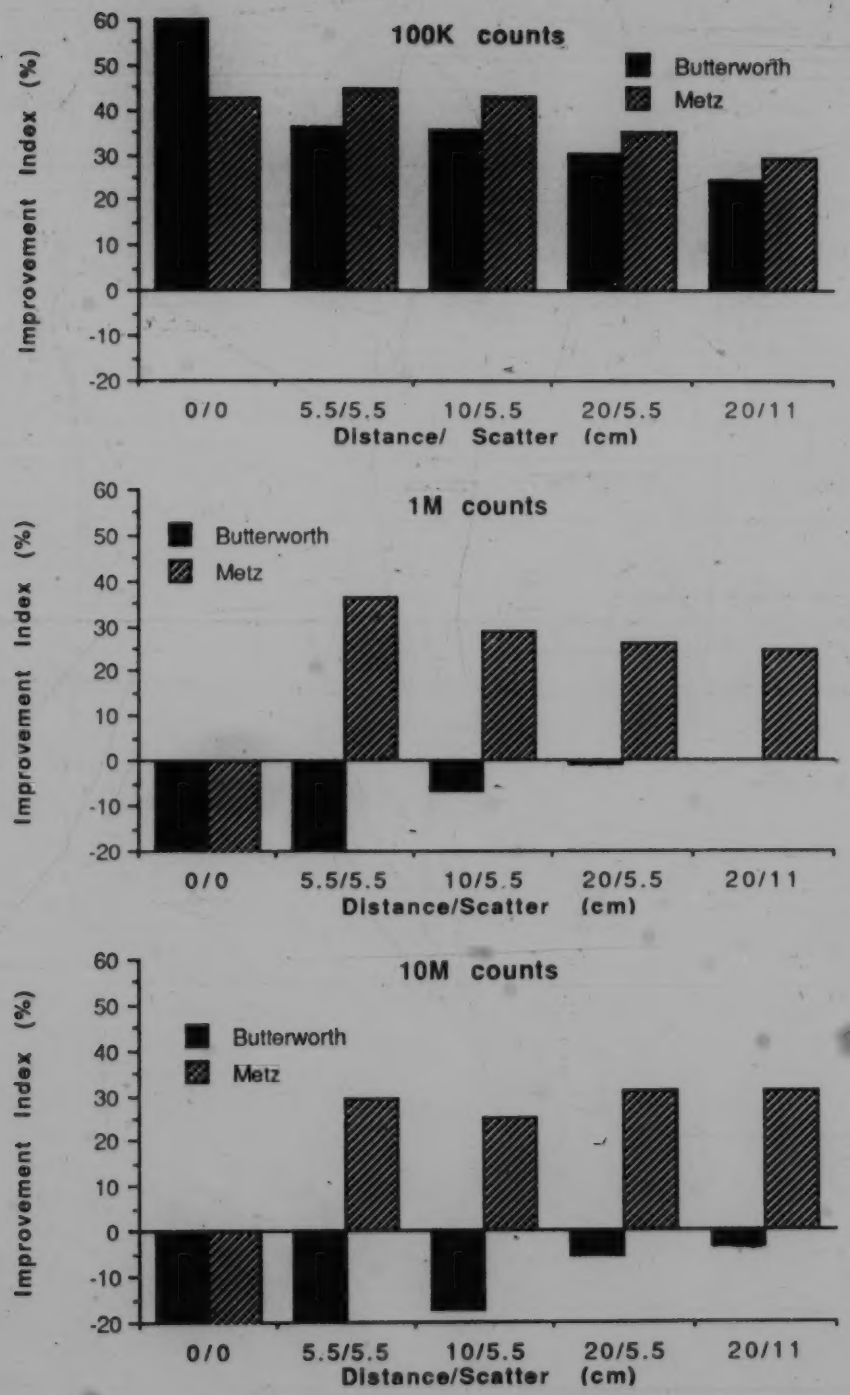

Figure 5.25 Improvement index of Butterworth and Metz filtered, technetium filled test phantom images.

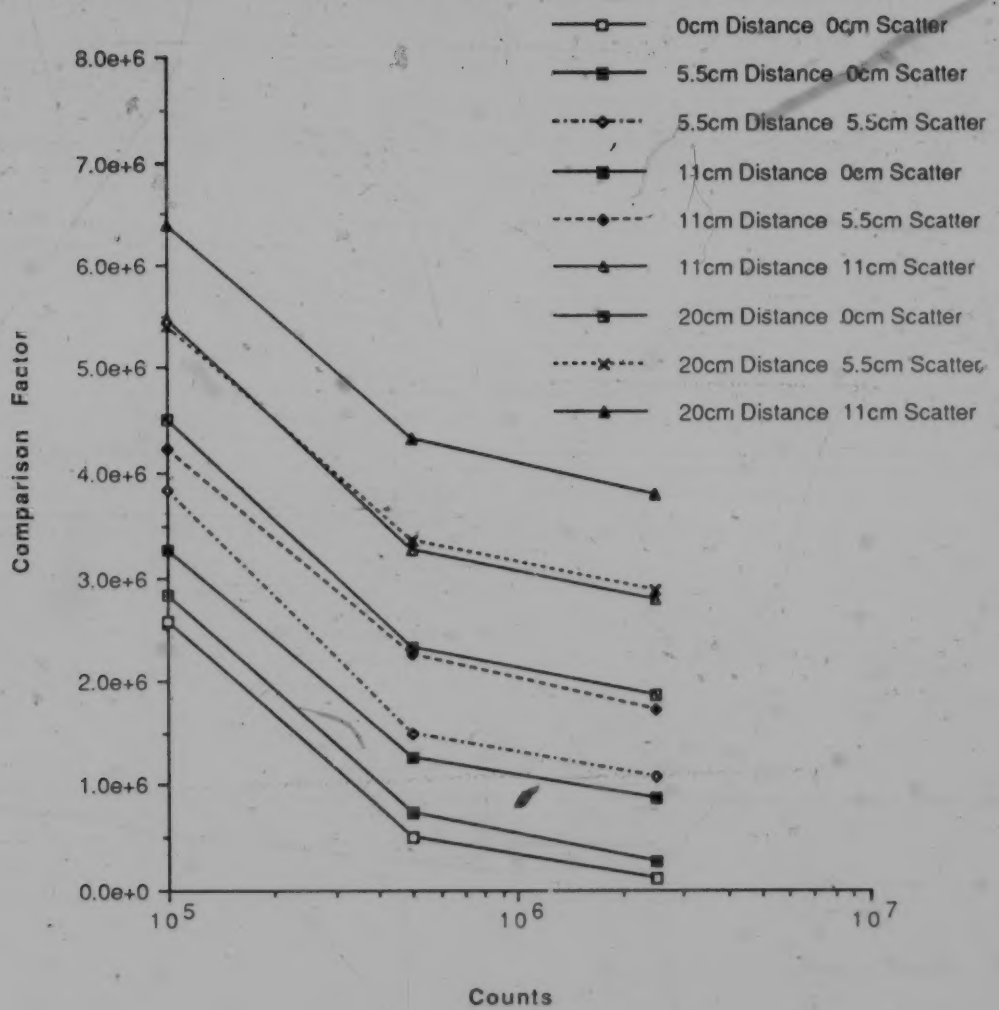

Figure 5.26 Comparison factor for raw indium filled test phantom images acquired under various conditions plotted as a function of counts.

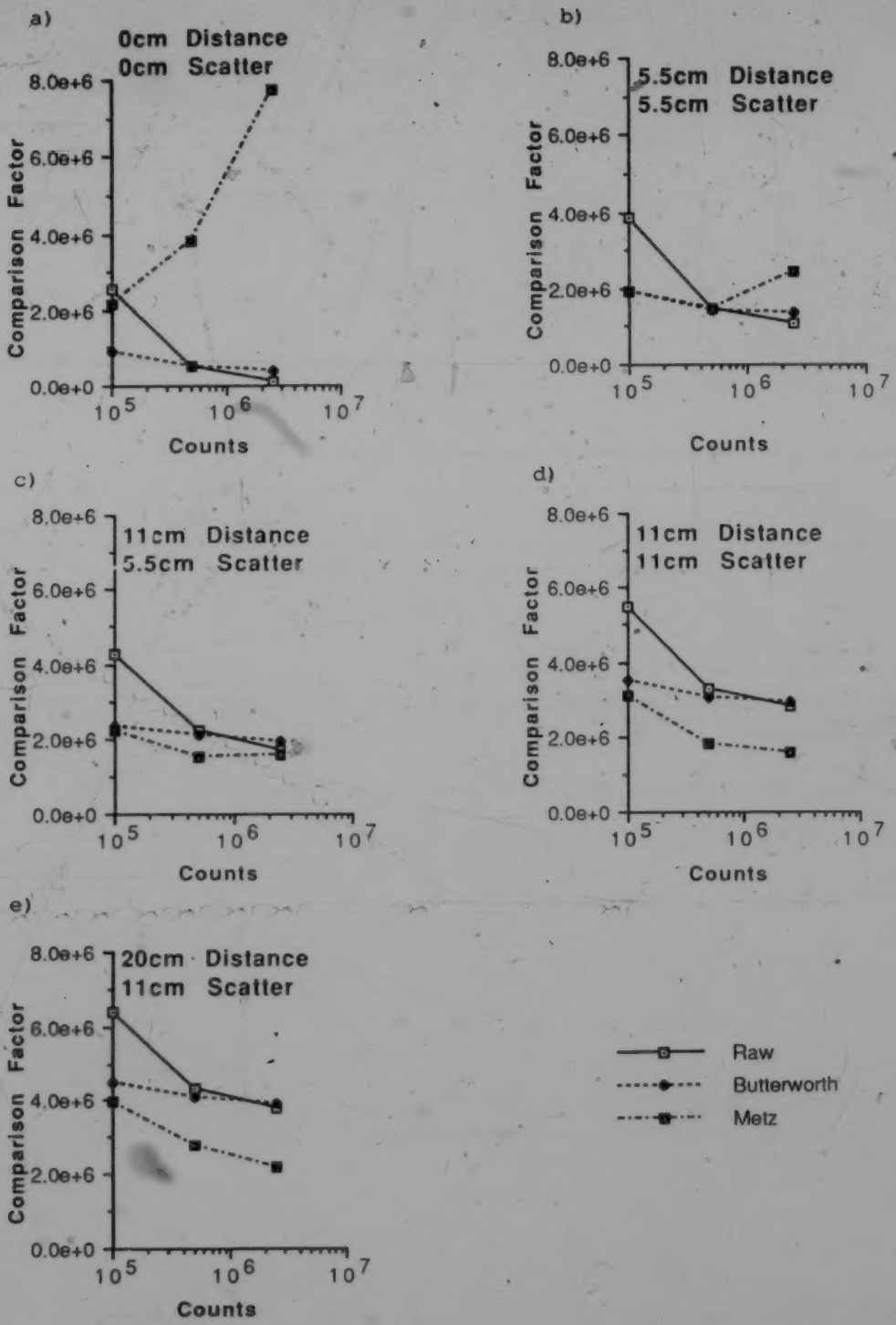

Figure 5.27 Effect of Butterworth and Metz filters on comparison factor of indium filled test phantom images.

Figure 5.28 shows the improvement index of the filtered indium images for various counts.

5.7 Discussion of Results

5.7.1 Noise

As seen in figures 5.3 and 5.4, the standard deviation of the pixel values in the raw flood images decreased as count increased. The noise, modelled by the inverse square root of the pixel value, was also plotted in the graphs. At low counts, the modelled noise line rose slightly above the raw flood's data point. The pixels had an average value of about three. At this value, the standard deviation of the noise could no longer be approximated by the inverse square root of the pixel count.

At high counts, the standard deviation of the noise images became much greater than the inverse square root approximation. This deviation from strictly Poisson noise occurred because, at high counts, the noise was dominated by spatial non-uniformities caused by collimator defects and, to a lesser extent, intrinsic camera non-uniformities.

The GE gamma camera has built in energy and spatial linearity corrections, calibrated using a technetium source. The raw indium flood images had slightly higher standard deviations at high counts than the raw technetium floods because the corrections are not as accurate at energies far away from the correction energy.

Filtering almost always decreased the standard deviation of the pixels. For the Metz filter with F_C/F_N equal to 0.5, the standard

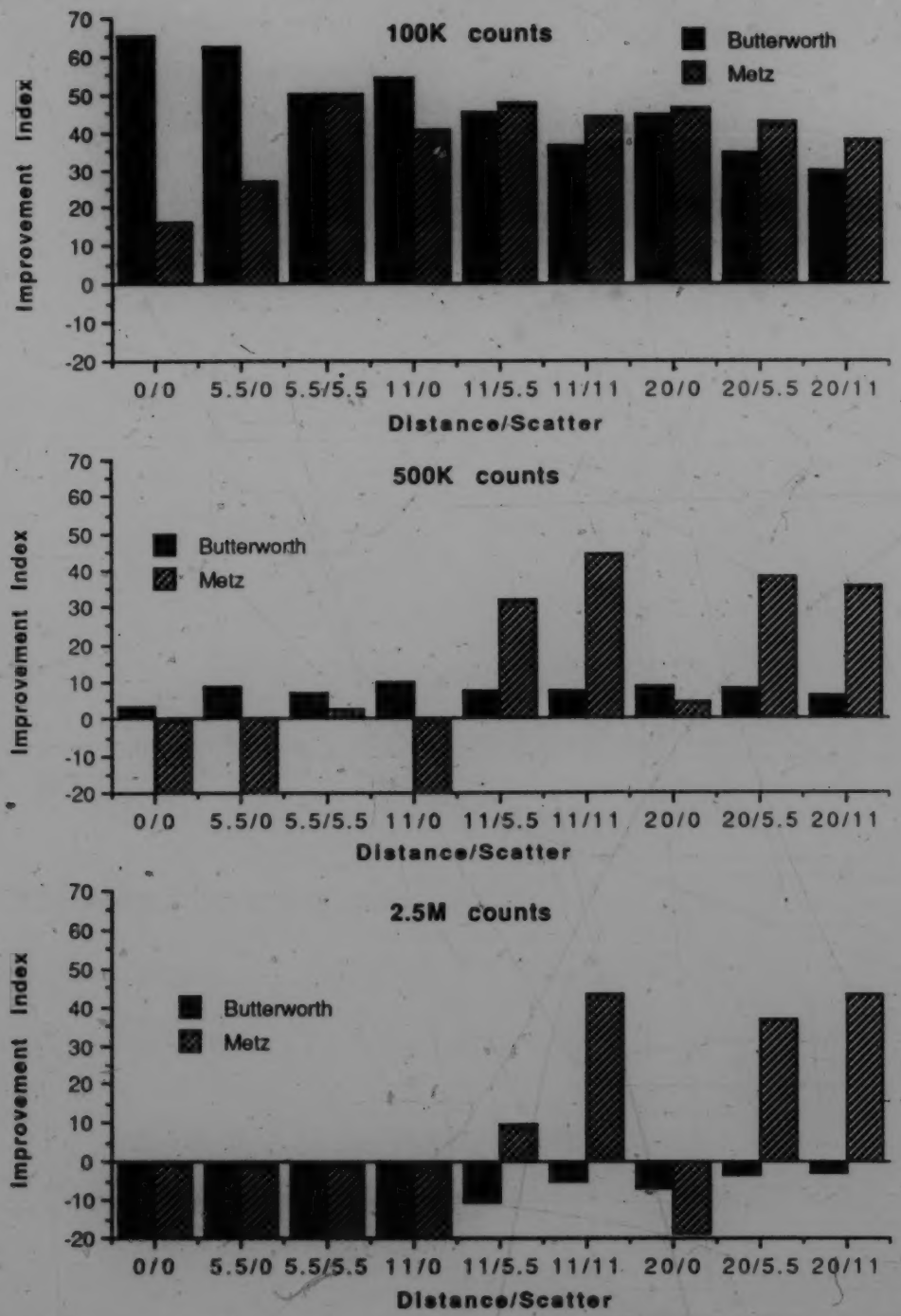

Figure 5.28 Improvement index of Butterworth and Metz filtered, indium filled test phantom images.

deviation of the pixel counts in the indium images actually increased at high counts. The Metz filter is an enhancing filter, and thus the spatial non-uniformities that dominate these images at high counts were enhanced.

Recall from Chapter IV, that the cutoff frequency of the Butterworth filter was $0.48 \cdot F_N$. The Butterworth filter's cutoff frequency is defined as the point where the response of the filter drops to fifty percent of the original unfiltered response. The Metz filter's cutoff parameter, F_c, is defined as the point where the filter's frequency response returns to 1.0 after boosting the lower frequency components. Therefore, the Butterworth filter's cutoff frequency cannot be directly compared to the Metz filter's cutoff parameter. As the cutoff parameter increases, the standard deviation of the pixel values also increases.

Figures 5.3 and 5.4 can be used to approximate the amount of noise in a region of a filtered image.

5.7.2 Contrast and Comparison Tests

As seen in figures 5.8 and 5.16, the contrast of the hot and cold spots increased in magnitude as counts decreased. This held for all distance/ scatter combinations. The contrast measured in images was thus partially dependent on noise. This dependence can be explained by noting that the contrast was measured by choosing the maximum or minimum pixel from a small group of pixels at the centre of a hot or cold spot. It is the fact that a single pixel was chosen from a larger group of pixels which biased the results.

Consider, for example, the cold spot contrast in which the

minimum pixel was chosen from a region of pixels. If the region consisted of only one pixel, then the statistical distribution of the pixel values would be governed by Poisson statistics. As the number of pixels in a region was increased, however, the probability of obtaining lower values increased. Both the mean and the standard deviation of the picked values decreased as the number of pixels increased.

The amount of noise also affected the comparison test results. Figures 5.23 and 5.26 plot the comparison factor as a function of image count. As might be expected, the comparison factor, Ψ, increased as total count decreased.

The resolution of the camera had an effect on the tests as well. The limited resolution of the camera caused sharp edges to be blurred. If a contrast spot was large enough, the centre of the spot was not affected. However, if the spot was small, the blurring effect from the edges of the spot would overlap and decrease the pixel values near the centre. This is referred to as a partial volume effect. As figures 5.7 and 5.16 illustrate, even in the reference images the contrast decreased as spot size decreased.

The resolution of the camera with the LEGP collimator was better than the resolution with the MESP collimator. The FWHM of a technetium point spread function at 10cm with no scatter was about 12mm, as compared to 16mm for indium. Unfortunately, the technetium data could not be compared directly to the indium data because the orientation of the phantom was different. For the indium images, the Plexiglas inserts were on the side away from the camera, whereas for the technetium images the inserts were on the side towards the camera.

Photons from cold regions travelling through the Plexiglas inserts in the technetium experiments were subject to greater attenuation, and hence the cold spots were colder than in the indium experiments. The photons emitted from the hot regions were attenuated by water, but the activity was distributed evenly throughout the water, and thus the hot region activity was similar in both sets of experiments. Therefore the contrast "seen" in the images was much greater in the technetium case that it was in the indium case.

Other imaging parameters affected the resolution of the imaging system. As the distance from the source to the camera increased, the resolution of the image decreased. This meant that the point spread function of the camera became flatter and broader. To isolate the effect that distance had on the images from the effect of noise, the highest count images were analyzed.

Figure 5.9 shows how the contrast of images changed as distance increased in the technetium images. The two largest contrast spots did not change significantly because they were large enough that their centres were not affected by the blurring of the edges. The smaller contrast spots demonstrate partial volume effects. Figure 5.17 shows how the contrast decreased with increasing distance in the medium energy images. Because of the poorer resolution of the indium images, the contrast decreased with distance in all but the largest contrast spot.

The effect of increasing distance on the comparison factor can be seen in figures 5.23 and 5.26 by looking at points with constant scatter. As the resolution decreases, the image becomes a poorer representation of the reference image and the comparison factor

increases.

The point spread function broadened when scattering material was added. For technetium, the FWHM of the point spread function of a test source at 10cm increased from 12mm with no scatter material to 13mm with 10cm of scattering material. However, the full width at tenth maximum (FWTM) increased from 21mm to 27mm. The broadening of the point spread function as scattering material was added caused the contrast in the images to decrease. This trend is illustrated in figure 5.10 for the technetium images, and in figure 5.18 for the indium images. Again, high count images were used to minimize the effect of noise.

The comparison factor increased as the amount of scattering material increased as seen in figures 5.23 and 5.26 by looking at points with a constant source to camera distance. Again, the blurring caused the comparison factor to increase.

The effect of filters on the contrast and the comparison test was studied. The first filter considered was a standard Butterworth filter. It is a smoothing filter; noise is suppressed but spatial resolution is also lost. The contrast is not expected to change for large contrast spots, but is expected to decrease for the smaller spots where partial volume effects are observed. Since, as discussed above, the comparison factor decreases as the noise decreases, but increases as the resolution decreases, the effect of this filter on comparison factor is difficult to predict.

The Butterworth filter used in this study had a somewhat sharp roll off and thus produced "ringing" at edges in the spatial domain. Figure 5.29a shows, in one dimension, the effect of filtering an edge

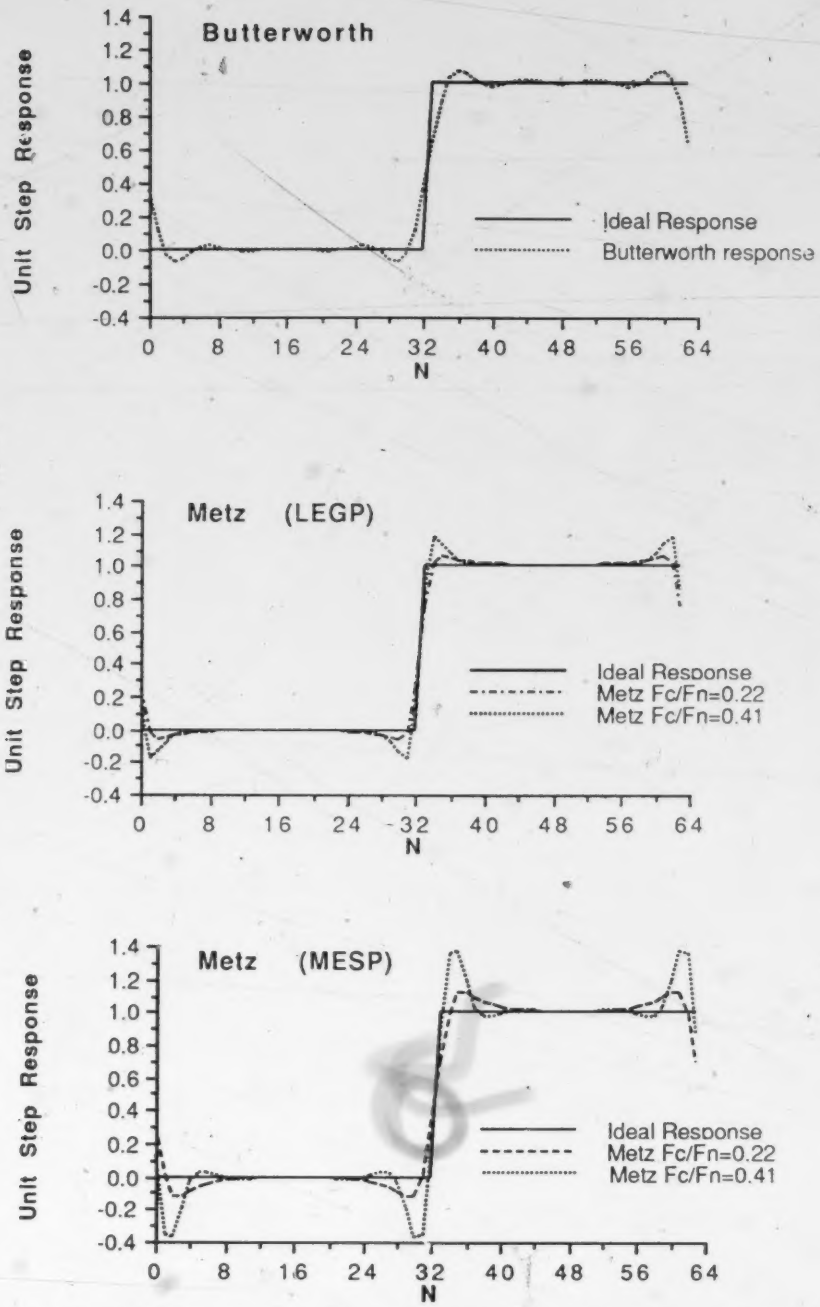

Figure 5.29 Unit step response of a) Butterworth filter, b) low energy collimator Metz filters, and c) medium energy collimator Metz filters. The axis, N, represents the pixel number where each pixel is 0.6cm wide.

with this Butterworth filter. The effect of these ripples was seen as ringing at sharp edges in the filtered image. Unfortunately, a contrast spot is more than a single edge. It has an edge all the way around it, and ripples from all these edges interact. Depending on the size of the contrast spot, the edge effects may interact constructively or destructively. The effects of the ripples were seen mostly in the 0cm distance, high count images. Note, for example, that in figure 5.11 the 6.0cm spot has a lower contrast than the 3.8cm spot. These images contained large high frequency components that were reduced by using the filter. At farther distances, or with more scatter, the images contained fewer high frequency components and the filter had less effect on the objects in the image but successfully reduced the noise. In the clinical situation, there is always scatter and the distance from the organ to the camera face is usually 10cm or more.

The Metz filter was a resolution enhancing filter. It tended to sharpen edges. The effect of filtering an edge with a low energy and a medium energy Metz filter is shown in figure 5.29b and 5.29c. Note that the ripples were larger especially with higher cutoff frequencies, but the ripples damped out faster with the Metz filter than with the Butterworth filter.

Figure 5.11 shows the effect of these filters on the contrast of the 0cm, 10 million count technetium images. Note that the Butterworth filter decreased the contrast in all but the 3.8cm spot. The cutoff frequency parameter F_C/F_N of the Metz filter was 0.54. The Metz filter significantly boosted the contrast of all the contrast spots. However, the 6.0cm contrast spot was not boosted as much as

the rest of the spots due to the way in which the edge effects of the Metz filter interacted. Figure 5.19 illustrates this for the filtered indium images. The F_C/F_N for the Metz filter for this image was 0.50.

By decreasing the count the Metz filter performed quite differently. The cutoff frequency, F_C/F_N, values chosen by the Metz filter program decreased from 0.54 to 0.24 as the count was reduced from 10 million to 100 thousand. As the count decreased, the low pass term in the Metz filter became more dominant.

As seen in figure 5.12, at 0cm with 100 thousand counts, the Metz filter increased the contrast of the two largest spots while it decreased the contrast in the smaller spots. The Butterworth filter decreased the contrast of all the contrast spots. The 100 million count reference image contrast data are also plotted for comparison. Because of the low count, more noise contributed to higher measured contrast. Notice that even the raw data had higher contrast than the reference image. Figure 5.20 shows that the indium images behaved in a similar way.

In figure 5.24a, the comparison factors, Ψ, for the raw and filtered technetium images acquired at 0cm have been plotted as a function of count. The indium data are shown in figure 5.27a. As expected, both filters performed poorly at higher counts, since both filters degraded the images. The image power spectra of the 0cm images contained high frequency components that were cut off by the low pass nature of the filters. However, at low counts the high frequency components were dominated by noise and Ψ was improved by the low pass filtering process.

The Metz filter was optimized [Ki87] for clinical images, and

therefore images acquired at larger distances with scatter material inserted were studied. Figure 5.13 shows the hot and cold contrasts for the 100 thousand count, 10cm imaging distance with 5.5cm scatter for the technetium images. Even though the counts were low, the contrast of the raw image was less than that of the reference image. The Butterworth filter did not reduce the contrast of the spots significantly. The Metz filter boosted the contrast of the two largest spots to values close to the reference image image's contrast. The smaller spots were again not affected to any great extent.

For the indium image at 11cm with 5.5cm scatter, the Butterworth filter decreased the contrast of all the spots (figure 5.21). The Metz filter increased the contrast of the 6cm spot very slightly. The contrasts of the smaller spots were reduced by both filters although the Metz reduced the contrast less.

At a distance of 20cm with 11cm of scatter material, the contrast of the raw data was considerably lower than the reference contrast as shown in figures 5.14 and 5.22. The cutoff frequency chosen by the program was $0.24 \cdot F_N$ pixels^{-1} for the technetium and $0.23 \cdot F_N$ pixels^{-1} for indium. The Metz filters started to roll off at lower frequencies than the Butterworth filter. There was little resolution recovery with the Metz filter due to the relatively low frequency cutoff. The Metz filter therefore performed much like the Butterworth.

The comparison factor performance of the filters is plotted as a function of count in figure 5.24 for the technetium images and figure 5.27 for the indium images. With the presence of scatter and at 5.5cm or more away from the camera face, the Butterworth filter worked well at low counts but increased the comparison factor, Ψ, at higher

counts. Again as discussed before, low count images contained significant noise components that were reduced by a simple low pass filter. Under the same conditions, the Metz filter performed well because the idealized MTF used in the Metz filter more closely matched the images' power spectra.

Since the Metz filter was optimized for the clinical imaging situation, it should perform best at a distance 10cm to 20cm away from the camera in the presence of scattering material. The Butterworth, being a low pass filter, was expected to work best at low counts where the amount of noise was large.

Figure 5.25 shows the improvement index for the technetium images. At 10 million and 1 million counts, the Butterworth filter degraded all the technetium images. Although the Metz filter degraded the 0cm distance, 0cm scatter image, it improved the images acquired at 5.5cm or greater with 5.5cm or greater thickness of scatter material. The benefits of the resolution recovery of the Metz filter is clearly illustrated in these high count images. At 100 thousand counts, both filters improved the images. The low pass characteristics of both filters improved the images by reducing the noise but the Metz filter performed slightly better than the Butterworth because it recovered some of the resolution lost due to scatter and distance.

Figure 5.28 shows the improvement index for the indium images. As with the technetium case, the 2.5 million count indium images were degraded by the Butterworth filter. The Metz filter's resolution recovery worked at distances greater than 11cm with 5.5cm or more scatter.

With the 500 thousand count images, the Butterworth filter

improved all the images slightly by reducing the noise. However, the Metz filter improved the images with 5.5cm or more scatter. Again, the ability of the Metz filter to recover resolution worked especially well when the imaging distance was greater than 11cm.

With 100 thousand counts, both filters improved the indium images. With more than 5.5cm scatter, the Metz filter performed marginally better. The combination of resolution recovery with noise suppression in the Metz filter has proven to work well under clinical imaging conditions.

Section VI . Conclusions and Future Experiments

6.1 Conclusion

Digital signal processing procedures have become an important part of SPECT reconstruction. By optimizing the projection images, the quality of the reconstructed images is expected to improve. In the past the Butterworth filter has been used to suppress noise. Recently, an image dependent Metz filter which combines resolution recovery with noise suppression has been implemented in clinical studies.

In this study, noise, contrast and comparison tests were performed on flood and test phantom images for various imaging conditions. The images were filtered and the tests repeated to study the performance of the filters.

The noise test measured the standard deviation of the pixel values in flood images. The noise in the unfiltered images had Poisson characteristics except at high counts densities, where spatial non-uniformities dominated the noise calculations. In the filtered images, the noise suppression characteristics of both filters reduced the standard deviation values in all cases except for the Metz filtered, high count indium images, where spatial non-uniformities were amplified by the filter.

The contrast test measured the contrast of the hot and cold spots in the test phantom. In the unfiltered images, the contrast increased as the number of counts in the image decreased. However, as

resolution decreased, partial volume effects became more significant and the contrast of the smaller spots decreased. In the Butterworth filtered images, noise was suppressed and resolution was also lost resulting in a decrease in contrast. Under clinical imaging conditions, the Metz filter did not significantly improve the contrast, but it also did not decrease the contrast as much as the Butterworth filter did. Ringing occurred when the images acquired at the camera face were filtered using either filter. Clinical images have fewer high frequency components, however, and thus are less prone to these ripple artefacts.

The third test, the comparison test, gave a measure of an image's similarity to a reference image. As counts increased, the comparison factor for a particular set of imaging conditions asymptotically approached a lower limit. As the resolution and/or scatter increased, the images became less like the reference image and the comparison factor increased. As illustrated in the improvement index data, the Butterworth filter improved the images significantly only at low counts where the noise suppression characteristics of this filter were most effective. The Metz filter behaved much like the Butterworth in the low count images, acting primarily as a noise suppression filter. The idealized MTF used in the Metz filter must be "tuned" or "focussed" to match the imaging conditions under which the images were obtained. Since this filter was in fact designed for clinical imaging situations where the collimator is some distance from the patient and a lot of scattering material is present, it is not surprising that this filter did not perform well for images acquired at the collimator face. The improvement index graphs, figures 5.25 and 5.28 show that

the Metz filter significantly improved all the images acquired with scatter and/or acquired at distances of 10cm or more from the collimator face. For clinical imaging, the Metz filter is the better filter out of the two filters evaluated.

6.2 Future Developments

A complete set of images for technetium and indium has been acquired. This data set can be used to test, using the three tests discussed earlier, new filters or image processing techniques. When new filters are described in the literature, this data set and these analysis techniques can be used to quickly assess the utility of these filters. The image processing is also not limited to just filtering; non-stationary convolution kernels [Ki88] could be tested as well.

It may be possible to develop a better Metz filter with some "retuning." There are two aspects of the Metz filter that can be varied. The values used in the modelled MTF can be varied to optimize them for clinical imaging conditions. The selection of the roll off parameter, X, can also be optimized to balance the resolution recovery with noise suppression by minimizing the comparison factor of the filtered images.

The noise, contrast and comparison data should be extended to other routinely used isotopes such as ^{201}Tl, ^{67}Ga, ^{123}I, and ^{131}I. High energy isotopes like ^{131}I pose problems when SPECT acquisition is desired. The loss of resolution using the high energy collimator is significant. A medium energy collimator could be used with the high

energy isotope, but septal penetration becomes a problem. It is possible that the septal penetration effects can be deconvolved with an appropriate filter. The Metz filter with an MTF that is not circularily symmetric may be a reasonable solution to this problem.

Bibliography

[An84] Anger RT. The Anger scintillation camera - A review. In *Physics of Nuclear Medicine - Recent Advances*, Rao DV, Chandra R, and Graham M (eds) American Association of Physicists in Medicine, New York, 1984: 54-58

[At86] Attix FH. *Introduction to Radiological Physics and Radiation Dosimetry*. New York: John Wiley and Sons, Inc., 1986:125-138

[Br74] Brigham EO. *The Fast Fourier Transform*. Englewood Cliffs, NJ: Prentice-Hall, Inc., 1974

[Cr86] Croft B. *Single Photon Emission Computed Tomography*. Chicago: Year Book Medical Publishers Chicago, 1986:142

[Du84] Dudgeon DE Mersereau RM. *Multidimensional Digital Signal Processing*. Englewood Cliffs, NJ: Prentice-Hall, Inc., 1984:363-376

[He87] Heller SL, Goodwin PN. SPECT instrumentation: performance, lesion detection, and recent innovations. *Seminars in Nuclear Medicine*; 1987; 3:184-199.

[Ka88] Kak AC, Slaney M. *Principles of Computerized Tomographic Imaging*. New York: The Institute of Electrical and Electronics Engineers, Inc., 1988:49-75

[Ki83a] King MA, Doherty PW, Schwinger RB, Jacobs DA, Kidder RE, Miller TR. Fast count dependent digital filtering of nuclear medicine images: concise communication. *The Journal of Nuclear Medicine*, 1983; 11:1039-1045

[Ki83b] King MA, Doherty PW, Schwinger RB and Penney BC. A Wiener filter for nuclear medicine images. *Medical Physics*, 1983; 6:876-880

[Ki84] King MA, Schwinger RB, Doherty PW, Penney BC. Two dimensional filtering of SPECT images using the Metz and Wiener filters. *The Journal of Nuclear Medicine*, 1984; 11:1234-1240

[Ki86a] King MA, Schwinger RB, Penney BC. Variation of the count dependent Metz filter with imaging system modulation transfer function. *Medical Physics*, 1986; 2:139-149

[Ki86b] King MA, Schwinger RB, Penney BC, Doherty PW, Bianco JA. Digital restoration of indium-111 and iodine-123 SPECT images with optimized Metz filters. *The Journal of Nuclear Medicine*, 1986; 8:1327-1336

[Ki87] King MA, Glick SJ, Penney BC, Schwinger RB, Doherty PW. Visual optimization of SPECT preconstruction filtering. *The Journal of Nuclear Medicine*, 1987; 7:1192-1198

[Ki88] King MA, Miller TR, Doherty PW, Schwinger RB. Stationary and nonstationary spatial domain Metz filtering. *Nuclear Medicine Communications*, 1988; 9:3-13

[Lu86] Ludeman LC. *Fundamentals of Digital Signal Processing*. New York: Harper and Row Publishers, Inc., 1986

[Ne86] National Electrical Manufacturers Association. *Performance Measurements of Scintillation Cameras*. Washington, DC: National Electrical Manufacturers Association, 1986:1-43

[So87] Sorensen JA, Phelps ME. *Physics in Nuclear Medicine Second edition;* Orlando, Florida: Grune and Stratton, Inc., 1987:72-78

[Ta82] Taylor JR. *An Introduction to Error Analysis - The Study of Uncertainties in Physical Measurement*. Mill Valley, California: University Science Books, 1982:207-237

[Te80] Ter-Pogossian MM, Raichle ME, Sobel BE. Positron Emission Tomography. *Scientific American*, 1980; 4:171-181

[We78] Webster JG (editor); *Medical Instrumentation - Application and Design;* Boston, Mass: Houghton Mifflin Company., 1978:593-600

Appendix I General Electric 400A Camera Specifications

-crystal size 9.5mm by 450mm (diameter)

-61 hexagonal photomultiplier tubes

-Auto tune automatically adjusts photomultiplier tube gains for detector stability

-"On the fly" energy and spatial distortion correction

-Three energy peaks with symmetric and asymmetric window capability

-Tomographic ring gantry stand

Appendix I continued

Parameter	(U/C)FOV	FW(H/T)M	WORSE CASE
Intrinsic Spatial Resolution	UFOV	FWHM	≤4.0mm
		FWTM	≤7.6mm
	CFOV	FWHM	≤3.9mm
		FWTM	≤7.6mm
@75,000 cps	UFOV	FWHM	≤4.5mm
System Spatial Resolution (LEGP)			
without scatter	-	FWHM	≤9.7mm
		FWTM	≤17.5mm
with scatter	-	FWHM	≤9.7mm
		FWTM	≤22.6mm
Intrinsic Energy Resolution	UFOV	FWHM	≤11.9%
	CFOV	FWHM	≤11.7%
Intrinsic Flood Field Uniformity (corrected)			
Integral (maximum deviation)	UFOV	-	≤±7.0%
	CFOV	-	≤±5.0%
Differential (maximum rate	UFOV	-	≤±4.0%
of change)	CFOV	-	≤±4.0%
Integral @75,000 cps	UFOV	-	≤±7.0%
Point Source Sensitivity	-	-	≤±4.0%
Intrinsic Spatial Linearity			
Absolute	UFOV	-	≤1.0mm
	CFOV	-	≤0.8mm
Differential	UFOV	-	≤0.3mm
	CFOV	-	≤0.5mm
System Sensitivity (cps/MBq; LEGP)	-	-	≥152cps/MBq
Intrinsic Count Rate Performance			
20% count loss rate (modes M/N/H)	-	-	≥65/75/105k cps
Maximum count rate	-	-	≥200k cps
Incident vs. observed	-	-	N/A
Multiple Window Spatial Registration	CFOV	-	≤2.0mm
Field of View (100mm from collimator)			
Imaging	UFOV	-	390mm
Testing	UFOV	-	370mm
	CFOV	-	278mm

UFOV-Largest inscribed circle in collimated FOV
CFOV- Circular area at 75% of UFOV diameter
Measured in accordance with NEMA Standards Publication for Performance Measurements of Scintillation Cameras No. NU1-1980

Mode N(normal)value fulfills required NEMA specification. Mode M (multiple window) and H (High Count Rate) values are not required per NEMA but are presented as supplementary information